Journal of Computational Physics **171,** 448–478 (2001)
doi:10.1006/jcph.2001.6779, available online at http://www.idealibrary.com on IDEAL®

Transparent Boundary Conditions for MHD Simulations in Stratified Atmospheres

A. Dedner,*,[1] D. Kröner,* I. L. Sofronov,†,[2] and M. Wesenberg*,[3]

**Institute for Applied Mathematics, University of Freiburg, Freiburg, Germany;*
and †Keldysh Institute of Applied Mathematics RAS, Moscow, Russia
E-mail: dedner@mathematik.uni-freiburg.de, dietmar@mathematik.uni-freiburg.de,
wesenber@mathematik.uni-freiburg.de, sofronov@spp.keldysh.ru

Received August 2, 2000; revised March 9, 2001

In this paper we discuss a method of deriving artificial nonreflecting boundary conditions for systems of conservation laws. We focus on an application from solar physics. The governing equations are the equations of ideal compressible magnetohydrodynamics (MHD), which are solved in a gravitationally stratified atmosphere. We derive the necessary equations, discuss implementational aspects, and show the effectiveness and efficiency of our boundary conditions in test calculations.

Key Words: MHD equations; solar physics; conservation laws; open boundaries; transparent boundary conditions; far-field linearization.

1. INTRODUCTION

Numerical simulations have become an important tool for improving our understanding of basic physical processes. Many applications of this type involve systems of conservation laws and are formulated either in infinite domains or in domains which are very large in comparison with the relevant structures. Even in the second case it can be almost impossible to find a formulation of the problem which is suitable for numerical simulations: If we perform the simulations in the whole domain with sufficient resolution to capture the small-scale structures, we waste a great deal of computational effort in uninteresting regions. Therefore, the size of the computational domain has to be severely reduced. This leads to artificial boundaries without physical meaning. In order to close the system of PDEs we have to find suitable boundary conditions on these boundaries. These artificial boundary

---

[1] Supported by DFG priority research program ANumE under Grant Kr795/11-2.

[2] Supported by RFBR Grant 01-01-00520 and University of Freiburg.

[3] Supported by DFG priority research program ANumE under Grant Kr795/11-2.

0021-9991/01 $35.00

conditions have to guarantee that the solutions in the truncated domain are as close as possible to those obtained in the whole domain.

One of the physical processes mentioned above is the time-periodic variation in solar activity. Its strength can be measured by the number and size of sunspots. Solar physicists suggest the following model to explain their formation: In the lower convection zone, the magnetic field concentrates in local tube-like structures within a stratified background atmosphere. Because of magnetic buoyancy these so-called flux tubes rise to the photosphere if their fragmentation is prevented by a sufficiently strong magnetic field tangential to their boundary; their outbreak at the sun's surface causes the visible sunspots. Hence the evolution of these flux tubes has become a focus of research in recent years; see, e.g., [6, 7, 13, 15, 27].

The simulation of rising magnetic flux tubes requires the numerical solution of the ideal compressible magnetohydrodynamic (MHD) equations. We use an explicit finite volume scheme with approximate Riemann solvers at the cell interfaces [11]. The computational domain is a portion of the solar convection zone with artificial vertical and horizontal boundaries. As in many applications requiring long-time simulations, the problem of finding suitable boundary conditions on these open boundaries has not yet been solved satisfactory. On one hand, small structures have to be resolved and their evolution has to be tracked over a long time period; on the other hand, the computational domain has to be chosen as small as possible to minimize computational costs. It would be desirable that all boundaries—the vertical as well as the horizontal ones—be transparent for outgoing waves. But since the dominant movement is the *rise* of the tube, the top boundary is the most critical one; the influence of the vertical boundaries is much smaller. For instance, in [13] both vertical boundaries and the bottom boundary are assumed to be "closed lids." According to [24] also the bottom boundary should be transparent. In the present study, we therefore focus our attention on both horizontal boundaries, while we assume periodic vertical boundaries in accordance with [6, 15, 24]. Our foremost concern is the derivation and validation of transparent boundary conditions that are designed with the above application in mind. The details of the physical assumptions and of the choice of the mathematical model are beyond the scope of this paper and we consider them to be "input data" from solar physics.

The conditions on the horizontal boundaries should lead to solutions which are (practically) independent of the height of the computational domain. Waves generated in the interior of the computational domain must be allowed to pass through the top and bottom boundary; i.e., an ideal artificial boundary should be transparent for outgoing perturbations. One method of achieving this is to absorb the outgoing waves by introducing additional layers at the boundaries. (For solar physical simulations this method was used in [13, 24].) As far as we know there is neither an analytical argument nor a detailed numerical study which shows that this approach meets the stated requirement for a non-reflecting boundary in the case of our application. However, the idea of absorbing layers seems to be a promising approach. This has recently been demonstrated for many different problems in the form of "perfectly matched layers;" see, e.g., [1, 5, 25, 32].

Our method of formulating nonreflecting boundary conditions belongs to the class of so-called exact boundary conditions (cf. the reviews [16, 31]). It follows the technique presented in [30], and develops ideas presented in [3, 17–19, 21, 23, 28, 29], where the derivation of boundary conditions is considered for different hyperbolic problems. Our method is based on the derivation of an analytically exact boundary condition for the hyperbolic equation describing the evolution of the pressure perturbation. The condition necessarily includes a term that is *non-local* with respect to time at the artificial boundaries. However, by using a special approximation this non-local term can be evaluated in a time-stepping manner so that the numerical method stays *local* with respect to time. Preliminary results of our research can be found in [10].

A necessary first step in the derivation of our boundary conditions is the linearization of the MHD equations about a stratified background atmosphere—for other nonlinear problems this approach was used, for example, in [4, 14, 23, 26, 30]. We assume that the perturbations at the boundary are sufficiently small and smooth. Furthermore, we study the special case of an exponentially decaying atmosphere. This choice is quite reasonable from the physical point of view [8, 20] and permits a sufficiently far-reaching analytical study. At the same time, the application of our boundary conditions to other models of the background atmosphere inside the computational domain seems to pose no problems. After deriving the boundary conditions and proving their correctness for the linearized system, we discuss implementational aspects and compare them with other more direct approaches. Our numerical examples illustrate that the structure of the solution is considerably influenced by the choice of the boundary conditions. Moreover, using our boundary conditions we find that even large perturbations are hardly reflected at the artificial boundaries. The examples indicate that the proposed transparent boundary conditions yield good results and are very cheap with respect to their computational costs.

2. GOVERNING EQUATIONS

The equations of ideal MHD describe the flow of an electrically conducting fluid under the influence of a magnetic field. They are obtained from the Euler equations of gas dynamics and the Maxwell equations if relativistic, viscous, and resistive effects are neglected. They are given by the following system of PDEs:

$$\partial_t \rho + \nabla \cdot (\rho \mathbf{u}) = 0 \tag{1a}$$

$$\partial_t (\rho \mathbf{u}) + \nabla \cdot (\rho \mathbf{u}\mathbf{u}^T + \mathcal{P}) = \rho \mathbf{g} \tag{1b}$$

$$\partial_t \mathbf{B} + \nabla \times (\mathbf{B} \times \mathbf{u}) = 0 \tag{1c}$$

$$\partial_t e + \nabla \cdot (e\mathbf{u} + \mathcal{P}\mathbf{u}) = \rho \mathbf{g} \cdot \mathbf{u} \tag{1d}$$

$$\nabla \cdot \mathbf{B} = 0. \tag{1e}$$

The total pressure tensor $\mathcal{P}$ is given by

$$\mathcal{P} = \left(p + \frac{1}{8\pi}|\mathbf{B}|^2\right)\mathcal{I} - \frac{1}{4\pi}\mathbf{B}\mathbf{B}^T; \tag{2}$$

$\mathbf{g} = \mathbf{g}(z) = (0, 0, g(z))^t$ with $g(z) < 0$ is a prescribed function describing the gravitational force, which acts in negative z-direction. Using an equation of state for the pressure (with the constant adiabatic exponent $\gamma > 1$)

$$p = (\gamma - 1)\left(e - \frac{1}{2}\rho|\mathbf{u}|^2 - \frac{1}{8\pi}|\mathbf{B}|^2\right), \tag{3}$$

the system can be rewritten as a hyperbolic system in the unknowns density ρ, momentum $\rho\mathbf{u}$, magnetic field $\mathbf{B}$, and total energy e. From (1c) we get $\partial_t(\nabla \cdot \mathbf{B}) = 0$, which allows us to regard (1e) as an initial condition.

3. GEOMETRY AND FORMULATION OF THE PROBLEM

We simplify the original solar physical problem in the following way: First, assuming that the computational domain is small compared with the whole convection zone, we use Cartesian (rather then spherical) coordinates (x, y, z) as in [13, 27]. Second, the computational domain is considered to be an elementary cell within a periodical structure along the x- and y-axes. Moreover, we restrict ourselves to a two-dimensional situation; i.e., we assume that all quantities depend on x, z, t and are independent of y. Therefore all y-derivatives in (1a)–(1e) vanish identically.

The domain of interest represents a sufficiently thin layer in the whole convection zone. Therefore it is convenient to consider our computational domain Ω_{comp} to be a portion of the infinite "well" $\Omega := \Omega_{bot} \cup \Omega_{comp} \cup \Omega_{top}$ (see Fig. 1),

$$\Omega := [0, x_r] \times (-\infty, \infty), \tag{4a}$$

$$\Omega_{comp} := [0, x_r] \times [z_b, z_t], \tag{4b}$$

$$\Omega_{bot} := [0, x_r] \times (-\infty, z_b], \tag{4c}$$

$$\Omega_{top} := [0, x_r] \times [z_t, \infty), \tag{4d}$$

with artificial horizontal boundaries

$$\Gamma_{bot} := \Omega_{comp} \cap \Omega_{bot}, \tag{5a}$$

$$\Gamma_{top} := \Omega_{comp} \cap \Omega_{top}. \tag{5b}$$

The governing equations described in the preceding section are considered in Ω_{comp}, and we assume that the initial conditions for the unknown functions differ from a static background atmosphere only inside this domain.

We prescribe periodic conditions on the vertical boundaries according to the simplifications made above. The main aim of the present study is to find boundary conditions on Γ_{top} and Γ_{bot} that permit us to regard these boundaries as *transparent* for waves generated during the simulation. Assuming that strong perturbations of the background atmosphere and strong nonlinear phenomena occur only inside the computational domain, we use a linearization of the governing equations about the background atmosphere in Ω_{top} and Ω_{bot}. The desired boundary conditions on Γ_{top} and Γ_{bot} are obtained through a rigorous analysis of this linear model in the far-field domain $\Omega \backslash \Omega_{comp}$.

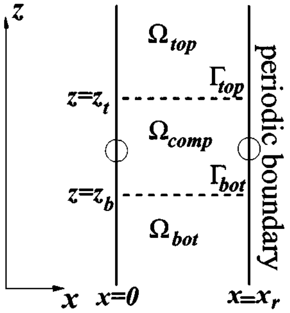

FIG. 1. Computational domain Ω_{comp}, far-field domains Ω_{top}, Ω_{bot} and artificial boundaries Γ_{top}, Γ_{bot}.

4. LINEARIZATION

In order to linearize (1a)–(3) in Ω_{top} and Ω_{bot}, we split the unknown quantities $\rho, \mathbf{u} = (u, v, w)^t, \mathbf{B}$, and p into background values (which are assumed to depend only on z) and perturbations:

$$\begin{aligned} \rho(t,x,z) &= \mathring{\rho}(z) + \tilde{\rho}(t,x,z), \\ \mathbf{u}(t,x,z) &= \mathring{\mathbf{u}}(z) + \tilde{\mathbf{u}}(t,x,z), \\ p(t,x,z) &= \mathring{p}(z) + \tilde{p}(t,x,z), \\ \mathbf{B}(t,x,z) &= \mathring{\mathbf{B}}(z) + \tilde{\mathbf{B}}(t,x,z). \end{aligned} \tag{6}$$

The perturbations $\tilde{\rho}$, $\tilde{\mathbf{u}}$, $\tilde{p}$, $\tilde{\mathbf{B}}$ are assumed to be small (acoustic perturbations) and must not be confused with the strong perturbations considered to be initial data in Ω_{comp} (see the preceding section). For the background values we assume

$$\frac{d}{dz}\mathring{p}(z) = g(z)\mathring{\rho}(z), \tag{7}$$

$$\mathring{\mathbf{u}}(z) = 0, \qquad \mathring{\mathbf{B}}(z) = 0, \tag{8}$$

$$\mathring{p} = \mathring{\rho}^{\gamma}, \quad \gamma = \text{const}, \tag{9}$$

with $g(z)$ and γ as introduced in the governing equations (1a)–(3). Due to (7) and (9) the function $g(z)$ and thus all background values are uniquely determined if $\mathring{\rho}(z)$ and γ are chosen. Evidently, the functions $\mathring{\rho}$, $\mathring{\mathbf{u}}$, $\mathring{\mathbf{B}}$, $\mathring{p}$ are a static solution to (1a)–(3).

Noting that the linearization of (3) yields

$$\tilde{p} = (\gamma - 1)\tilde{e}, \tag{10}$$

we obtain from (1a)–(3) the system of equations for the perturbations

$$\partial_t \tilde{\rho} + \mathring{\rho}\partial_x \tilde{u} + \partial_z(\mathring{\rho}\tilde{w}) = 0, \tag{11a}$$

$$\mathring{\rho}\partial_t \tilde{u} + \partial_x \tilde{p} = 0, \tag{11b}$$

$$\mathring{\rho}\partial_t \tilde{w} + \partial_z \tilde{p} - \tilde{\rho} g = 0, \tag{11c}$$

$$\partial_t \tilde{p} + \gamma \mathring{p}(\partial_x \tilde{u} + \partial_z \tilde{w}) + \mathring{\rho} g \tilde{w} = 0 \tag{11d}$$

and

$$\partial_t \tilde{v} \equiv 0, \tag{12a}$$

$$\partial_t \tilde{\mathbf{B}} \equiv 0. \tag{12b}$$

We see that under the assumptions of (7) and (8) the linear MHD equations are reduced to Eq. (12a) and (12b) and the system (11a)–(11d) for the gasdynamic unknowns $\tilde{\rho}, \tilde{u}, \tilde{w}, \tilde{p}$. Equations (12a) and (12b) can already be used as boundary conditions for $\tilde{v}$ and $\tilde{\mathbf{B}}$ on Γ_{top} and Γ_{bot}; therefore we have to analyze only the system (11a)–(11d).

For the derivation of the transparent boundary conditions we fix the following initial and boundary conditions for (11a)–(11d) in the far field:

- homogeneous initial data

$$\tilde{\rho},\, \tilde{u},\, \tilde{w},\, \tilde{p}|_{t=0} = 0 \quad \text{in } \Omega_{top} \text{ and } \Omega_{bot}, \tag{13}$$

- boundedness of pressure perturbations at infinity

$$|\tilde{p}| < \infty \quad \text{at } z = +\infty, \tag{14a}$$

$$|\tilde{p}| < \infty \quad \text{at } z = -\infty, \tag{14b}$$

- conditions of periodicity on the vertical boundaries of Ω.

5. EQUATION FOR THE PRESSURE PERTURBATION $\tilde{p}$

To provide the desired analysis, we pass from system (11a)–(11d) to a scalar equation. From (11a) and (11d) we have

$$\partial_t \tilde{p} - \gamma \frac{\mathring{p}}{\mathring{\rho}} \partial_t \tilde{\rho} + \tilde{w}\left(\mathring{\rho} g - \gamma \frac{\mathring{p}}{\mathring{\rho}} \partial_z \mathring{\rho} \right) = 0.$$

The Eq. (7) and (9) give us

$$\partial_z \mathring{\rho} = \frac{\mathring{\rho}}{\gamma \mathring{p}} \mathring{\rho} g;$$

hence

$$\partial_t \tilde{p} - \gamma \frac{\mathring{p}}{\mathring{\rho}} \partial_t \tilde{\rho} = 0. \tag{15}$$

Using (13), we obtain from (15) that

$$\tilde{p} = \gamma \frac{\mathring{p}}{\mathring{\rho}} \tilde{\rho}. \tag{16}$$

Differentiating (11b) and (11d) w.r.t. x and t, respectively, we have

$$\partial^2_{tt} \tilde{p} + \gamma \mathring{p} \partial^2_{zt} \tilde{w} - \gamma \frac{\mathring{p}}{\mathring{\rho}} \partial^2_{xx} \tilde{p} + \mathring{\rho} g \partial_t \tilde{w} = 0. \tag{17}$$

To exclude $\partial^2_{zt} \tilde{w}$, $\partial_t \tilde{w}$ from (17), we use (11c); then

$$\partial^2_{tt} \tilde{p} + \gamma \mathring{p} \left(\partial_z \left(\frac{g \tilde{\rho}}{\mathring{\rho}} \right) - \partial_z \left(\frac{\partial_z \tilde{p}}{\mathring{\rho}} \right) \right) - \frac{\gamma \mathring{p}}{\mathring{\rho}} \partial^2_{xx} \tilde{p} + g(g\tilde{\rho} - \partial_z \tilde{p}) = 0.$$

Relationship (16) permits us to exclude $\tilde{\rho}$ from this equation. Finally we have the following equation for $\tilde{p}$:

$$\partial^2_{tt} \tilde{p} - \frac{\gamma \mathring{p}}{\mathring{\rho}} \left(\partial^2_{zz} \tilde{p} + \partial^2_{xx} \tilde{p} \right) + g \partial_z \tilde{p} + \left(\partial_z g - \frac{\gamma - 1}{\gamma} g^2 \frac{\mathring{\rho}}{\mathring{p}} \right) \tilde{p} = 0. \tag{18}$$

It is convenient to introduce the function

$$q(z) := \frac{\gamma}{\gamma - 1}\mathring{\rho}(z)^{\gamma-1} \tag{19}$$

and the constant

$$\vartheta := (\gamma - 1)^{-1}.$$

Then, because of (7) and (9), the coefficients of (18) are expressed in terms of q; in particular,

$$g(z) = q'(z). \tag{20}$$

Thus Eq. (18) takes the form

$$\partial_{tt}^2 \tilde{p} - \vartheta^{-1} q\left(\partial_{zz}^2 \tilde{p} + \partial_{xx}^2 \tilde{p}\right) + q' \partial_z \tilde{p} + q\left(\frac{q'}{q}\right)' \tilde{p} = 0. \tag{21}$$

Note the following expression for the speed of sound $\mathring{c} \equiv \sqrt{\gamma \mathring{p}/\mathring{\rho}}$ in the background atmosphere: $\mathring{c}(z) = \sqrt{q(z)/\vartheta}$.

To find the general solution to (21), we have to specify the function $q(z)$, which also serves to define the background values (7)–(9) used for the system (11a)–(11d) except for the constant γ. In the following we provide our analysis for the particular case of an exponentially decaying atmosphere:

ASSUMPTION 5.1. *Let $q(z)$ be of the form*

$$q(z) = a^{-1} e^{-2\alpha z}, \tag{22}$$

where $a > 0, \alpha > 0$ are some constants.

It is easy to see from (9) and (19) that (22) describes an exponential law for the background pressure and density, which are uniquely defined if $a,\ \alpha$, and γ are chosen. In particular we find

$$\mathring{c}(z) = e^{-\alpha z}/\sqrt{a\vartheta}. \tag{23}$$

Remark. The special choice of q permits us to advance far enough with purely analytical methods to obtain exact boundary conditions. (This seems to be impossible in the general case.) At the same time, such a choice is not exotic: On the one hand, an exponential atmosphere is a suitable model in several physical situations (see [8, 20]). On the other hand, it is possible to use a different background atmosphere, e.g., governed by a power law, inside Ω_{comp} with a smooth transition to exponential atmospheres in Ω_{top} and Ω_{bot}. (Note that we can use different exponential atmospheres in the two far-field domains.) We will address this topic in a forthcoming paper.

6. BOUNDARY CONDITIONS FOR $\tilde{p}$ ON Γ_{top}

Using Fourier transformation w.r.t. x—see (40a)—we pass from (21) to equations for the harmonics $\tilde{p}^\lambda(t, z)$ with a corresponding eigenvalue λ:

$$\partial_{tt}^2 \tilde{p}^\lambda - \vartheta^{-1} q\left(\partial_{zz}^2 \tilde{p}^\lambda - \lambda^2 \tilde{p}^\lambda\right) + q' \partial_z \tilde{p}^\lambda + q\left(\frac{q'}{q}\right)' \tilde{p}^\lambda = 0. \tag{24}$$

The Laplace transformation $\tilde{p}^\lambda(t, z) \mapsto \hat{p}^\lambda(z)$ reduces (24) to an ordinary differential equation with parameter $s \in [0, \infty)$ (the hat ˆ denotes the dependency on s):

$$s^2 \hat{p}^\lambda - \vartheta^{-1} q \left(\partial_{zz}^2 \hat{p}^\lambda - \lambda^2 \hat{p}^\lambda\right) + q' \partial_z \hat{p}^\lambda + q \left(\frac{q'}{q}\right)' \hat{p}^\lambda = 0. \tag{25}$$

Substituting (22) for q in (25), we have

$$\partial_{zz}^2 \hat{p}^\lambda + 2\alpha\vartheta \partial_z \hat{p}^\lambda - (\lambda^2 + as^2 \vartheta e^{2\alpha z}) \hat{p}^\lambda = 0. \tag{26}$$

This equation is reduced to the modified Bessel equation,

$$y^2 f'' + y f' - (y^2 + \nu^2) f = 0 \tag{27}$$

by the substitutions

$$\hat{p}^\lambda(z) = e^{\delta z} f(be^{\beta z}), \quad y = be^{\beta z},$$
$$\delta = -\alpha\vartheta, \quad \beta = \alpha, \quad b = \frac{s}{\alpha}\sqrt{a\vartheta},$$
$$\nu^2 = \left(\frac{\lambda}{\alpha}\right)^2 + \vartheta^2.$$

Because of (14a), the desired solution to (27) is the Macdonald function $K_\nu(\sigma)$ that decays as $\sigma \to \infty$ (see [2]). Therefore, the general solution to (26) has the form

$$\hat{p}^\lambda(z) = Ce^{-\alpha\vartheta z} K_\nu(\alpha^{-1}\sqrt{a\vartheta} e^{az} s), \tag{28}$$

where C is an arbitrary constant. To exclude this constant, we calculate the derivative $\frac{d}{dz}\hat{p}^\lambda$ from (28) and obtain the relationship

$$\frac{d}{dz}\hat{p}^\lambda(z) = -\hat{B}_{top}^\lambda(s, z)\hat{p}^\lambda(z) \quad \text{at } z = z_t, \tag{29}$$

where

$$\hat{B}_{top}^\lambda(s, z) := \alpha\vartheta - \sqrt{a\vartheta} e^{\alpha z} s \frac{K_\nu'(\alpha^{-1}\sqrt{a\vartheta} e^{az} s)}{K_\nu(\alpha^{-1}\sqrt{a\vartheta} e^{\alpha z} s)}. \tag{30}$$

Now we extract those terms from (30) that do not decay as $s \to \infty$. If we introduce the function

$$\hat{A}_{top}^\lambda(s, z) := \alpha^{-1}\sqrt{a\vartheta} e^{\alpha z} s \left(\frac{K_\nu'(\alpha^{-1}\sqrt{a\vartheta} e^{\alpha z} s)}{K_\nu(\alpha^{-1}\sqrt{a\vartheta} e^{\alpha z} s)} + 1 + \frac{1}{2\alpha^{-1}\sqrt{a\vartheta} e^{\alpha z} s}\right), \tag{31}$$

(30) is equivalent to

$$\hat{B}_{top}^\lambda(s, z) = \sqrt{a\vartheta} e^{\alpha z} s + \alpha\vartheta + \frac{\alpha}{2} - \alpha\hat{A}_{top}^\lambda(s, z). \tag{32}$$

Because of the identity

$$K'_\nu(\sigma) = -K_{\nu+1}(\sigma) + \frac{\nu K_\nu(\sigma)}{\sigma}, \tag{33}$$

we may rewrite (31) as

$$\hat{A}^\lambda_{top}(s, z) = \hat{\mathcal{A}}^\nu_{top}(\sigma) := -\sigma\frac{K_{\nu+1}(\sigma)}{K_\nu(\sigma)} + \nu + \sigma + \frac{1}{2} \tag{34}$$

with

$$\sigma := \alpha^{-1}\sqrt{a\vartheta}e^{\alpha z}s. \tag{35}$$

Using asymptotic properties of $K_\nu(\sigma)$ for large σ, we have

$$-\frac{K'_\nu(\sigma)}{K_\nu(\sigma)} = 1 + \frac{1}{2\sigma} + O\left(\frac{1}{\sigma^2}\right)$$

(see [2]). Thus (31) decays to 0 as $s \to \infty$. We denote by $A^\lambda_{top}(t, z)$ the inverse Laplace transformation of $\hat{A}^\lambda_{top}(s, z)$:

$$A^\lambda_{top}(t, z) := \mathcal{L}^{-1}\left[\hat{\mathcal{A}}^\nu_{top}(\sigma)\right](\tau) \quad \text{with } \tau := t\alpha/(\sqrt{a\vartheta}e^{\alpha z}). \tag{36}$$

To show that $A^\lambda_{top}(t, z)$ exists, we have to consider analytical properties of $\hat{\mathcal{A}}^\nu_{top}(\sigma)$. The zeros σ_j of $K_\nu(\sigma)$ have negative real parts

$$\operatorname{Re}\sigma_j < \sigma_\nu < 0 \tag{37}$$

(see [2]). Therefore $\hat{\mathcal{A}}^\nu_{top}(\sigma)$ is analytical for $\operatorname{Re}\sigma \geq \sigma_\nu$. Since

$$\hat{\mathcal{A}}^\nu_{top}(\sigma) = -\frac{4\nu^2 - 1}{8}\frac{1}{\sigma} + O\left(\frac{1}{\sigma^2}\right),$$

the conditions for the existence of the inverse Laplace transformation (36) are satisfied, (see, e.g., [22]); moreover, we have the estimate

$$\mathcal{L}^{-1}\left[\hat{\mathcal{A}}^\nu_{top}(\sigma)\right](\tau) = O(e^{\sigma_\nu \tau}) \to 0 \quad \text{as } \tau \to \infty. \tag{38}$$

Now we can use (36) to obtain from (29) and (32) the equation at $z = z_t$ for each Fourier coefficient $\tilde{p}^\lambda(t, z)$

$$\sqrt{a\vartheta}e^{\alpha z}\partial_t\tilde{p}^\lambda + \partial_z\tilde{p}^\lambda + \left(\alpha\vartheta + \frac{\alpha}{2}\right)\tilde{p}^\lambda - \frac{\alpha^2}{\sqrt{a\vartheta}}e^{-\alpha z}\int_0^t A^\lambda_{top}(t - t', z)\tilde{p}^\lambda(t', z)\,dt' = 0,$$

or in a more convenient form (taking (23) into account)

$$\partial_t\tilde{p}^\lambda + \mathring{c}\,\partial_z\tilde{p}^\lambda + \left(\alpha\vartheta + \frac{\alpha}{2}\right)\mathring{c}\,\tilde{p}^\lambda - \alpha^2\mathring{c}^2 A^\lambda_{top} * \tilde{p}^\lambda = 0. \tag{39}$$

Denote by Q and Q^{-1} the operators of direct and inverse Fourier transformation w.r.t. x, respectively; i.e.,

$$f^{\lambda_k} := (Qf)(\lambda_k) := \frac{1}{x_r}\int_0^{x_r} e^{i\lambda_k x} f(x)\,dx, \quad k = 0, \pm 1, \pm 2, \ldots, \tag{40a}$$

$$f(x) := \left(Q^{-1}\left\{\left(f^{\lambda_k}\right)_{k\in\mathbb{Z}}\right\}\right)(x) := \sum_{k=-\infty}^{\infty} f^{\lambda_k} e^{-i\lambda_k x}, \quad \lambda_k = \frac{2\pi}{x_r}k, \tag{40b}$$

where x_r is the width of the well (see Fig. 1). Then the set of conditions (39) for different values of λ can be written in physical space as follows:

$$\partial_t \tilde{p} + \mathring{c}\,\partial_z \tilde{p} + \left(\alpha\vartheta + \frac{\alpha}{2}\right)\mathring{c}\,\tilde{p} - \alpha^2 \mathring{c}^{\,2} Q^{-1}\left\{A_{top}^{\lambda_k} *\right\} Q\tilde{p} = 0 \quad \text{at } z = z_t. \tag{41}$$

The notation $\{A_{top}^{\lambda_k} *\}$ is used to stress that the convolution kernel for each Fourier coefficient f^{λ_k} depends on λ_k. This is the desired nonreflecting condition for (21) on Γ_{top}. We shall not prove this statement here since our goal is to analyze the system (11a)–(11d), not the scalar equation (21); nevertheless, some test calculations for (41) are contained in Section 10.

7. BOUNDARY CONDITIONS FOR (11a)–(11d) ON Γ_{top}

Using (11c) we exclude the derivative w.r.t. z from (41). Thus the desired nonreflecting condition for (11a)–(11d) at $z = z_t$ has the form

$$\partial_t \tilde{p} - \mathring{c}\mathring{\rho}\,\partial_t \tilde{w} + \left(\alpha\vartheta + \frac{\alpha}{2}\right)\mathring{c}\,\tilde{p} + \mathring{c}g\tilde{\rho} - \alpha^2 \mathring{c}^{\,2} Q^{-1}\left\{A_{top}^{\lambda_k} *\right\} Q\tilde{p} = 0. \tag{42}$$

In order to prove this, let us consider the following two linear problems for the vector of unknowns $\tilde{\mathbf{V}} = (\tilde{\rho}, \tilde{u}, \tilde{w}, \tilde{p})$ in (11a)–(11d) and a given function $\tilde{\mathbf{V}}^0$ with supp $\tilde{\mathbf{V}}^0 \subset \Omega_{comp}$: Equations (11a)–(11d) in the infinite domain Ω with

- the initial conditions $\tilde{\mathbf{V}}_0 = \begin{cases} 0 & \text{in } \Omega_{top} \cup \Omega_{bot} \\ \tilde{\mathbf{V}}^0 & \text{in } \Omega_{comp} \end{cases}$ and (A)
- the boundary conditions $|\tilde{\mathbf{V}}| < \infty$ for $z \to \pm\infty$;

Equations (11a)–(11d) in $\Omega \backslash \Omega_{top}$ with

- the initial conditions $\tilde{\mathbf{V}}_0 = \begin{cases} 0 & \text{in } \Omega_{bot} \\ \tilde{\mathbf{V}}^0 & \text{in } \Omega_{comp} \end{cases}$ and (B)
- the boundary conditions $\begin{cases} |\tilde{\mathbf{V}}| < \infty & \text{for } z \to -\infty \\ (42) & \text{on } \Gamma_{top} \end{cases}$.

For both problems the parameters $\mathring{\rho}$, $\mathring{p}$, and g in (11a)–(11d) are defined through the background atmosphere (7)–(9) using (19) with q according to (22). The vertical boundaries are assumed to be periodic.

THEOREM 7.1.

1. *Any solution to problem* (A) *is a solution to problem* (B).
2. *Let us consider a solution to problem* (B), *which is continuously differentiable up to* Γ_{top}. *Then it is possible to prolong it into* Ω_{top} *to obtain a solution to problem* (A).

Proof. The first statement is evident since we derived (42) from the representation of a general solution to (11a)–(11d); i.e., (42) is valid for functions which satisfy (11a)–(11d). Let us prove the second statement. First we write out the prolongation formulae. Let $\tilde{\mathbf{V}} = (\tilde{\rho}, \tilde{u}, \tilde{v}, \tilde{p})$ be a solution to problem (B). We fix a time t, denote by $p_{\Gamma_{top}}(t, x)$ the trace of $\tilde{p}$ on Γ_{top}, and calculate its image $\hat{p}^{\lambda}_{\Gamma_{top}}(s) := \mathcal{L}Qp_{\Gamma_{top}}$. From (28) we find that

$$\hat{p}^{\lambda}(s, z) = \hat{p}^{\lambda}_{\Gamma_{top}}(s) e^{-\alpha\vartheta(z - z_t)} \frac{K_\nu(\alpha^{-1}\sqrt{a\vartheta}e^{\alpha z}s)}{K_\nu(\alpha^{-1}\sqrt{a\vartheta}e^{\alpha z_t}s)}, \quad z > z_t. \tag{43}$$

Because $K_\nu(C\sigma)/K_\nu(\sigma) \sim e^{(1-C)\sigma}$ and we have $C > 1$ in (43), the inverse Laplace transformation of $\hat{p}^{\lambda}(s, z)$ exists. Therefore, calculating the inverse Laplace and Fourier transformations of $\hat{p}^{\lambda}(s, z)$ in (43), we obtain the function $\tilde{p}(t, x, z)$ in Ω_{top}. The remaining functions in Ω_{top} are expressed in terms of $\tilde{p}(t, x, z)$ by using (11b), (11c), (13), and (16):

$$\tilde{u} = -\frac{1}{\mathring{\rho}} \int_0^t \partial_x \tilde{p}\, dt, \tag{44}$$

$$\tilde{w} = -\frac{1}{\mathring{\rho}} \int_0^t \partial_z \tilde{p} - g\tilde{\rho}\, dt, \tag{45}$$

$$\tilde{\rho} = \frac{\mathring{\rho}}{\gamma \mathring{p}} \tilde{p}. \tag{46}$$

We have to prove that our functions $\tilde{p}, \tilde{u}, \tilde{w}, \tilde{\rho}$ satisfy (11a)–(11d) in Ω_{top}. Formulae (44) and (45) immediately give (11b) and (11c). Let us prove (11d). A direct calculation using (44)–(46), (18) yields

$$\begin{aligned}
&\partial_t \tilde{p} + \gamma \mathring{p}(\partial_x \tilde{u} + \partial_z \tilde{w}) + \mathring{\rho} g \tilde{w} \\
&\quad = \partial_t \tilde{p} - \frac{\gamma \mathring{p}}{\mathring{\rho}} \int_0^t \partial^2_{xx} \tilde{p} + \partial^2_{zz} \tilde{p} - \partial_z(g\tilde{\rho})\, dt + \gamma \mathring{p} \frac{\partial_z \mathring{p}}{\mathring{p}^2} \int_0^t (\partial_z \tilde{p} - g\tilde{\rho})\, dt + \mathring{\rho} g \tilde{w} \\
&\quad = \partial_t \tilde{p} - \int_0^t \partial^2_{tt} \tilde{p} + g\partial_z \tilde{p} + \left(\partial_z g - \frac{\gamma - 1}{\gamma} g^2 \frac{\mathring{\rho}}{\mathring{p}}\right) \tilde{p}\, dt + \frac{\gamma \mathring{p}}{\mathring{\rho}} \int_0^t \partial_z(g\tilde{\rho})\, dt \\
&\qquad + g \int_0^t \partial_z \tilde{p} - g\tilde{\rho} + \mathring{\rho}\partial_t \tilde{w}\, dt \\
&\quad = \int_0^t \frac{\gamma \mathring{p}}{\mathring{\rho}} \partial_z(g\tilde{\rho}) - g\partial_z \tilde{p} - \tilde{p}\partial_z g + \frac{\gamma - 1}{\gamma} g^2 \frac{\mathring{\rho}}{\mathring{p}} \tilde{p}\, dt \\
&\quad = 0.
\end{aligned}$$

A similar direct calculation proves (11a). Thus it follows that (11a)–(11d) are valid in $\Omega \backslash \Omega_{top}$ and Ω_{top}; it remains to be proved that they are valid on Γ_{top}, i.e., at $z = z_t$. Since $\tilde{p}$ is continuously differentiable at $z = z_t$, the derivative $\partial_t \tilde{u}$ calculated by (11b) from the upper and lower side of Γ_{top} has the same value; therefore (11b) is valid at $z = z_t$. We see that $\tilde{u}$ is continuous w.r.t. z at $z = z_t$; the function $\tilde{\rho}$ is also continuous (see (46)); therefore (11a) is valid at $z = z_t$. Using (11c) and (42) in $\Omega \backslash \Omega_{top}$, we pass to (41) and calculate $\partial_z \tilde{p}$ on Γ_{top} from the lower side. On the other hand, since (41) is valid for $\tilde{p}$ defined by (43) in Ω_{top}, we can calculate $\partial_z \tilde{p}$ from the upper side by using (41) as well. Because $\tilde{p}$ is continuously differentiable on Γ_{top}, both values of $\partial_z \tilde{p}$ are the same; i.e., $\partial_z \tilde{p}$ is continuous at $z = z_t$.

Hence (11c) is valid on Γ_{top}. This yields the continuity of $\tilde{w}$ w.r.t. z at $z = z_t$. Therefore (11d) is also valid at $z = z_t$. ■

This theorem allows us to use the condition (42) on Γ_{top} and to solve the governing equations just in $\Omega \backslash \Omega_{top}$ instead of in the whole domain Ω. Although (42) is obtained from the linear analysis, we use it to close the nonlinear equations (1a)–(1d) in $\Omega \backslash \Omega_{top}$. We arrive at a complete set of equations on Γ_{top} if we add (11b), (16) and (11c):

$$\mathring{\rho}\partial_t \tilde{u} + \partial_x \tilde{p} = 0, \tag{47}$$

$$\tilde{\rho} - \mathring{c}^{-2}\tilde{p} = 0, \tag{48}$$

$$\mathring{\rho}\partial_t \tilde{w} + \partial_z \tilde{p} - \tilde{\rho} g = 0. \tag{49}$$

Here we used the speed of sound $\mathring{c}$ as introduced in Section 5.

8. THE BOTTOM BOUNDARY

For the bottom domain Ω_{bot} we have the same equation (26), but now the general solution is given by

$$\hat{p}^\lambda(z) = Ce^{-\alpha\vartheta z} I_\nu(\alpha^{-1}\sqrt{a\vartheta}e^{\alpha z}s), \quad \nu^2 = \left(\frac{\lambda}{\alpha}\right)^2 + \vartheta^2. \tag{50}$$

We use the Bessel functions $I_\nu(\sigma)$ because of their asymptotic behavior for small σ,

$$I_\nu(\sigma) \sim \sigma^\nu \quad \text{as } \sigma \to 0,$$

which yields

$$\hat{p}^\lambda(z) \sim e^{\alpha(\nu-\vartheta)z} < \infty \quad \text{as } z \to -\infty.$$

Thus (14b) is satisfied.

By formally making a similar analysis as in Section 7, we obtain the following boundary condition for (21) on Γ_{bot}:

$$\partial_t \tilde{p} - \mathring{c}\partial_z \tilde{p} - \left(\alpha\vartheta + \frac{\alpha}{2}\right)\mathring{c}\tilde{p} + \alpha^2 \mathring{c}^2 Q^{-1}\left\{A_{bot}^{\lambda_k} *\right\} Q\tilde{p} = 0 \quad \text{at } z = z_b. \tag{51}$$

Here we have used

$$A_{bot}^\lambda(t, z) := \mathcal{L}^{-1}\left[\hat{\mathcal{A}}_{bot}^\nu(\cdot)\right](\tau \mapsto t\alpha\mathring{c}(z)) \tag{52}$$

and (cf. (34))

$$\hat{\mathcal{A}}_{bot}^\nu(\sigma) := \sigma\frac{I_{\nu+1}(\sigma)}{I_\nu(\sigma)} + \nu - \sigma + \frac{1}{2} = \sigma\frac{I_\nu'(\sigma)}{I_\nu(\sigma)} - \sigma + \frac{1}{2}. \tag{53}$$

Now we have to check whether the inverse Laplace transformation (52) exists. For $\mu := 4\nu^2$ the function $I_\nu(\sigma)$ has the asymptotic expansion

$$I_\nu(\sigma) \sim \frac{e^\sigma}{\sqrt{2\pi\sigma}}\left(1 - \frac{\mu - 1}{8\sigma} + \frac{(\mu-1)(\mu-9)}{2!(8\sigma)^2} - \frac{(\mu-1)(\mu-9)(\mu-25)}{3!(8\sigma)^3} + \cdots\right)$$

as $|\sigma| \to \infty$ (see [2]). Substituting this expression into (53), we get (using MAPLE)

$$\hat{\mathcal{A}}^{\nu}_{bot}(\sigma) \sim (4\nu^2 - 1)\left(\frac{1}{8}\frac{1}{\sigma} + \frac{1}{8}\frac{1}{\sigma^2} + \cdots + \frac{n!}{2^n} p_n(\nu)\frac{1}{\sigma^n} + \cdots\right) \quad \text{as } \sigma \to \infty,$$

where $p_n(\nu)$ are polynomials of order less than n with bounded coefficients w.r.t. n.

Using the property of correspondence between asymptotic expansions of a function $f(\tau)$ as $\tau \to 0$ and its Laplace transformation $\mathcal{L}[f](\sigma)$ as $\sigma \to \infty$ (see, e.g., [12]), we find that the function formally defined in (52) has the asymptotic expansion

$$\mathcal{A}^{\nu}_{bot}(\tau) \sim (4\nu^2 - 1)\left(\frac{1}{8} + \frac{1}{8}\tau + \cdots + \frac{n}{2} p_n(\nu)\left(\frac{\tau}{2}\right)^{n-1} + \cdots\right) \tag{54}$$

as $\tau \to 0$. This series converges within the finite interval $0 \le \tau < 2$. Therefore, we can expect the existence of (52) only up to a finite time. To our knowledge, the current theory of Laplace transformation does not give an answer to the question of whether or not (52) actually exists.

Remark. For $\tau \ge 2$ we have to expect terms with generalized functions in (52). This is because the function (53) has an infinite number of purely imaginary poles with absolute values equal to the zeros of the Bessel function $J_\nu(\sigma)$ according to $I_\nu(\sigma) = i^{-\nu} J_\nu(i\sigma)$.

In order to understand the physical reason that an upper limitation with respect to time appears, let us analyze (24) in Ω_{bot} by using the theory of characteristics. Equation (24) is a hyperbolic equation with characteristics defined by

$$\frac{dz^\pm}{dt} = \pm\mathring{c}(z^\pm) = \pm e^{-az^\pm}/\sqrt{a\vartheta}, \tag{55}$$

where the local speed of sound $\mathring{c}$ is given by (23). Therefore $\mathring{c}(z) \to \infty$ as $z \to -\infty$. By integrating (55) for the characteristic going to $-\infty$ starting at the location of the bottom boundary z_b, we obtain

$$z^-(t) = z_b + \alpha^{-1}\ln(1 - \alpha\mathring{c}(z_b)t). \tag{56}$$

Thus a signal starting from $z = z_b$ arrives at $-\infty$ after the finite time

$$t_b = \frac{1}{\alpha\mathring{c}(z_b)}. \tag{57}$$

This value corresponds to the non-dimensional time $\tau = 1$ (see (52)). If we also take into account the time which a signal reflected at $-\infty$ needs to return to $z = z_b$, we have to multiply this value by 2. Hence we obtain the same upper bound $\tau = 2$ as in (54).

Remark. The problems we encounter during the derivation of our boundary conditions on Γ_{bot} are caused by the fact that the exponential atmosphere (22) used in Ω_{bot} is unbounded as $z \to -\infty$. However, we have refrained from using another model of the atmosphere since we want to remain in the framework developed for the top boundary. Note that even if the analysis is only valid up to a finite time, the approximation proposed in Section 9 works well even for far larger times, as the examples in Section 10 demonstrate.

Assuming the existence of (54), we continue our analysis for obtaining transparent boundary conditions on Γ_{bot} and get from (51) and (11c)

$$\partial_t \tilde{p} + \mathring{c}\mathring{\rho}\partial_t \tilde{w} - \left(\alpha\vartheta + \frac{\alpha}{2}\right)\mathring{c}\,\tilde{p} - \mathring{c}g\tilde{\rho} + \alpha^2\mathring{c}^{\,2}Q^{-1}\left\{A^{\lambda_k}_{bot}*\right\}Q\tilde{p} = 0. \tag{58}$$

The additional equations for the remaining functions are (cf. (47)–(49)):

$$\mathring{\rho}\partial_t \tilde{u} + \partial_x \tilde{p} = 0, \tag{59}$$

$$\tilde{\rho} - \mathring{c}^{-2}\tilde{p} = 0, \tag{60}$$

$$\mathring{\rho}\partial_t \tilde{w} + \partial_z \tilde{p} - \tilde{\rho}g = 0. \tag{61}$$

The statement that (58) is the desired boundary condition is formulated and proved quite similar to Theorem 7.1; one has to stress that the solutions are considered only within a finite time interval.

9. NUMERICAL IMPLEMENTATION

Both Eqs. (41) and (51) contain the non-local operators of Fourier transformation and convolution with respect to time. Computationally, the Fourier transformation is not too expensive, since we can use FFT algorithms. Because it suffices to treat only the first few Fourier harmonics by (41) and (51), we can even rely on simple discrete counterparts to (40a) and (40b). For the remaining shortwave harmonics, the non-local terms in these equations can be omitted because of their smaller contribution to the whole solution (cf. discussion in [29]). Computational resources are mainly required for the operators A^{λ}_{top} and A^{λ}_{bot} of convolution with respect to time. To reduce the costs, we explore the following approach: at first we approximate the convolution kernels by sums of exponentials; thereafter the recurrence formula for convolution integrals with exponential kernels is used:

$$I(t) := \int_0^t e^{\beta(t-t')} f(t')\,dt' = e^{\beta\tau} I(t-\tau) + \int_{t-\tau}^t e^{\beta(t-t')} f(t')\,dt'.$$

Due to this approach, the computational resources required by (42) and (58) are quite reasonable with respect to both computational time and storage.

9.1. *Approximation of the Convolution Kernels*

The approximation of the convolution kernels by exponential sums is made numerically. First we approximate the functions $\hat{\mathcal{A}}^{\nu}_{top}(\sigma)$ in (34) and $\hat{\mathcal{A}}^{\nu}_{bot}(\sigma)$ in (53) by rational functions

$$\hat{\mathcal{A}}^{\nu}_{n}(\sigma) := \frac{P_n(\sigma)}{Q_{n+1}(\sigma)}, \tag{62}$$

where $P_n(\sigma)$, $Q_{n+1}(\sigma)$ are polynomials of degrees n and $n+1$, respectively. (The value of n depends on the accuracy we need.) This approximation is made in advance by using the MAPLE package. We apply the Chebyshev–Padé algorithm, which consists of three consecutive stages:

1. approximate representation by Chebyshev polynomials:

$$\hat{\mathcal{A}}_n^\nu(\sigma) \approx a_0 + \sum_{k=1}^{N(n)} a_k T_k(\sigma);$$

2. application of the Padé algorithm to obtain the coefficients of a rational approximation:

$$a_0 + \sum_{k=1}^{N(n)} a_k \sigma^k \approx \frac{b_0 + \sum_{k=1}^{n} b_k \sigma^k}{c_0 + \sum_{k=1}^{n+1} c_k \sigma^k};$$

3. use of the Padé coefficients with the Chebyshev polynomials:

$$\hat{\mathcal{A}}_n^\nu(\sigma) \approx \frac{b_0 + \sum_{k=1}^{n} b_k T_k(\sigma)}{c_0 + \sum_{k=1}^{n+1} c_k T_k(\sigma)} =: \frac{P_n(\sigma)}{Q_{n+1}(\sigma)}.$$

An example of such a code for λ_1 is given in the Appendix. The inverse Laplace transformation of (62) turns out to be a sum of exponentials. Let $\beta_1, \ldots, \beta_{n+1}$ be the complex zeros of Q_{n+1}. Then we have

$$Q_{n+1}(\sigma) = \prod_{k=1}^{n+1} (\sigma - \beta_k). \tag{63}$$

Since

$$Q'_{n+1}(\sigma) = \sum_{l=1}^{n+1} \prod_{k \neq l} (\sigma - \beta_k), \tag{64}$$

we get

$$Q'_{n+1}(\beta_j) = \prod_{k \neq j} (\beta_j - \beta_k) \quad \forall j \in \{1, \ldots, n+1\}. \tag{65}$$

Now assume that $\beta_1, \ldots, \beta_{n+1}$ are pairwise distinct. Then we may define

$$b_j := \frac{P_n(\beta_j)}{Q'_{n+1}(\beta_j)} \quad \forall j \in \{1, \ldots, n+1\} \tag{66}$$

and we find

$$\begin{aligned} \sum_{j=1}^{n+1} \frac{b_j}{\sigma - \beta_j} &= \frac{1}{Q_{n+1}(\sigma)} \sum_{j=1}^{n+1} \left(\frac{P_n(\beta_j)}{Q'_{n+1}(\beta_j)} \prod_{k \neq j} (\sigma - \beta_k) \right) \\ &\overset{(65)}{=} \frac{1}{Q_{n+1}(\sigma)} \sum_{j=1}^{n+1} \left(P_n(\beta_j) \prod_{k \neq j} \frac{\sigma - \beta_k}{\beta_j - \beta_k} \right) \\ &=: \frac{R_n(\sigma)}{Q_{n+1}(\sigma)}. \end{aligned}$$

Since R_n has degree n,

$$R_n(\beta_j) = P_n(\beta_j) \quad \forall j \in \{1, \ldots, n+1\}$$

and $|\{\beta_1, \ldots, \beta_{n+1}\}| = n+1$, we have $R_n \equiv P_n$. With (62) this yields

$$\hat{\mathcal{A}}_n^\nu(\sigma) = \sum_{j=1}^{n+1} \frac{b_j}{\sigma - \beta_j}. \tag{67}$$

Because the inverse Laplace transformation $\mathcal{L}^{-1}$ is linear and fulfils

$$\mathcal{L}^{-1}\left[\frac{1}{\sigma - \beta}\right](\tau) = e^{\beta\tau}, \tag{68}$$

we end up with

$$A^\lambda \approx A_n^\lambda := \mathcal{L}^{-1}\left[\hat{\mathcal{A}}_n^\nu(\cdot)\right](\tau \mapsto \alpha\mathring{c}t) = \sum_{j=1}^{n+1} b_j e^{\alpha\mathring{c}\beta_j t}. \tag{69}$$

If we use this approximation for the kernel $\hat{A}_{top}^\lambda$, we obtain convergence for increasing n in numerical experiments. For instance, Fig. 2 (left) shows $A_{16}^\nu(\tau)$ with $\nu = 15.78$ and the deviation from the approximation with $n = 8$. This is the typical situation we observed within our computations for any value of ν.

However, for the bottom boundary the situation is quite different. Figure 2 (right) shows the approximations of the "bottom" kernel with the same $\nu = 15.78$ calculated for $n = 8, 12, 16$. There is no convergence; moreover, several values of β_j in (69) have positive real parts, which lead to divergence of the convolution integral. The reason for this behavior is clear from the analysis made in Section 8: the kernel $\hat{A}_{bot}^\lambda$ can be represented by a function only up to a finite time. (It is interesting to note that the graphs in Fig. 2 confirm this fact: they match each other in an initial finite interval.)

On the other hand, there is no restriction on the simulation time imposed by the top boundary. Evidently, the difficulty with the bottom boundary occurs because of the admission of

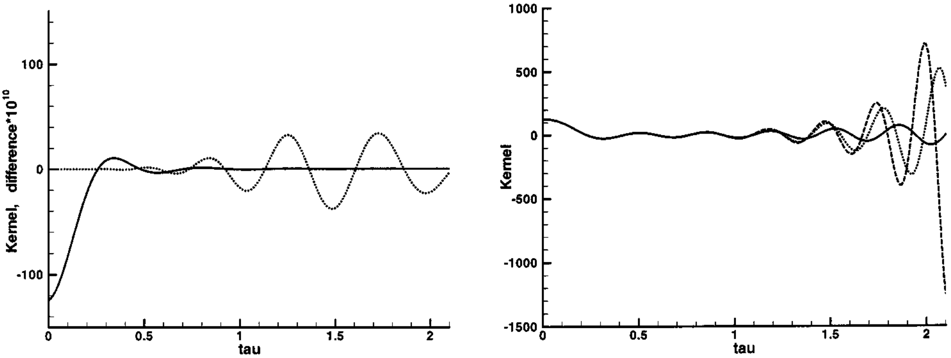

FIG. 2. $\nu = 15.78$. Top boundary (left): kernel $\mathcal{A}_{16}^\nu(\tau)$ (solid line), and the difference $\mathcal{A}_{16}^\nu(\tau) - \mathcal{A}_8^\nu(\tau)$ multiplied by 10^{10} (dotted line). Bottom boundary (right): kernels $\mathcal{A}_8^\nu(\tau)$ (solid line), $\mathcal{A}_{12}^\nu(\tau)$ (dotted line) and $\mathcal{A}_{16}^\nu(\tau)$ (dashed line).

nonphysical background functions which are unbounded as $z \to -\infty$. One possibility for overcoming this problem would be to change the law (22) in the vicinity of $z = -\infty$ (e.g., by putting $\alpha = 0$ for large $|z|$, $z < 0$). We propose another approach which permits us to remain in the framework of the method developed: we add the requirement that admissible exponential approximations to A^{λ}_{bot} have to be *bounded* for $0 \le t < \infty$. This means that we have to find a representation of the form (69) which approximates the "bottom" kernel along the initial time interval and which has no β_j with positive real parts (in order to keep the convolution integral stable in long-time simulations). We implement the following procedure to do this. Let us consider the function $I'_\nu(\sigma)/I_\nu(\sigma)$ in the complex plane. Since $I_\nu(\sigma) = i^{-\nu} J_\nu(i\sigma)$, the corresponding residues are easily computed:

$$\operatorname{Res}\frac{I'_\nu(\sigma)}{I_\nu(\sigma)} = 1 \quad \text{at } \sigma = \pm i a^k_\nu, \quad \text{where } J_\nu\left(a^k_\nu\right) = 0, \quad k = 1, 2, \ldots .$$

We fix an integer number $M \ge 1$ and form the rational function

$$\mathcal{R}^\nu_M(\sigma) := 2\sum_{k=1}^{M} \frac{\left(a^k_\nu\right)^2}{\sigma^2 + \left(a^k_\nu\right)^2},$$

whereby $a^1_\nu, \ldots, a^M_\nu \in \mathbb{R}$ are the first M positive roots of J_ν. Hence the auxiliary function

$$\left(\hat{\mathcal{A}}^\nu_{bot}\right)_M := \hat{\mathcal{A}}^\nu_{bot} + \mathcal{R}^\nu_M$$

has no poles in the circle $\{\zeta \in \mathbb{C} \mid |\zeta| < a^M_\nu\}$. As soon as we have constructed a representation of type (69) with $\operatorname{Re}\beta_j \le 0$ for $(\hat{\mathcal{A}}^\nu_{bot})_M$, the corresponding approximation to $\mathcal{A}^\nu_{bot}$ is obtained by simply subtracting the term

$$\mathcal{L}^{-1}\left[\mathcal{R}^\nu_M\right](\tau) = 2\sum_{k=1}^{M} a^k_\nu \sin\left(a^k_\nu \tau\right) = \sum_{k=1}^{M}\left(i a^k_\nu e^{-i a^k_\nu \tau} - i a^k_\nu e^{i a^k_\nu \tau}\right),$$

which is evidently bounded for $0 \le \tau < \infty$. Therefore, the approximation to $\mathcal{A}^\nu_{bot}$ is of the form (69) with bounded coefficients. Note that although the Laplace transformation is linear, this trick has an effect because the numerical procedure of computing $\{b_j, \beta_j\}$ is nonlinear. Without our modification, we obtained bounded approximations of $\mathcal{A}^\nu_{bot}$ only for very small values of n; n could not be chosen large enough to yield sufficiently transparent and stable boundary conditions. Our modification enables us to compute bounded approximations for an arbitrary value of n if $M \approx n$. (For small values of λ we had to choose M slightly larger than n.) These approximations lead to boundary conditions which are transparent and stable even in long-time simulations.

9.2. *Discretization of Transparent Boundary Conditions*

All boundary conditions (41), (47)–(49), (51), (59)–(61) are discretized in a similar manner. As an example, we consider Eq. (41), concentrating on one of the Fourier modes governed by (39). Let $\{b_j, \beta_j\}$ be the corresponding coefficients of the representation (69) for the kernel A^λ_{top} with a given λ. Substituting it in (39) and omitting ˜ and λ in the notation,

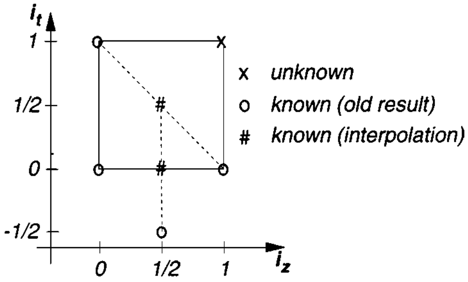

FIG. 3. Mesh for discretization.

we arrive at the equation

$$\partial_t p + \mathring{c}\,\partial_z p + \mathring{c}\left(\alpha\vartheta + \frac{\alpha}{2}\right)p - \alpha^2\mathring{c}^{\,2}\int_0^t \sum_{j=1}^{n+1} b_j e^{\alpha\mathring{c}\beta_j(t-t')}\,p(t',z)\,dt' = 0. \tag{70}$$

We discretize (70) on a grid stencil as sketched in Fig. 3 in the following manner:

- p_{i_t,i_z} denotes the discrete value of p at the grid point (t^{i_t}, z_{i_z}).
- The points at position z_0 are the last ones within the computational domain; those at z_1 are "ghost points."
- The "half" time and space levels are defined as usual:

$$t^{1/2} := \frac{1}{2}(t^0 + t^1), \quad t^{-1/2} := \frac{1}{2}(t^{-1} + t^0), \quad z_{1/2} := \frac{1}{2}(z_0 + z_1).$$

(Note that the boundary Γ_{top} is located at $z_t = z_{1/2}$.)

- We assume that the values within the computational domain are given (updated) up to time t^1, while the "ghost values" are known up to t^0 (including $p_{-1/2,1/2}$).
- To obtain $p_{1,1}$, we discretize (70) using central differences around $(t^{1/2}, z_{1/2})$.

For the discretization of (70) we set $\Delta t_{1/2} := t^1 - t^0$, $\Delta z := z_1 - z_0$ and choose the approximations

$$\partial_t p\big(t^{1/2}, z_{1/2}\big) \approx \frac{1}{\Delta t_{1/2}}\big(p_{1,1/2} - p_{0,1/2}\big) \approx \frac{1}{2\Delta t_{1/2}}(p_{1,0} + p_{1,1} - p_{0,0} - p_{0,1}), \tag{71a}$$

$$\partial_z p\big(t^{1/2}, z_{1/2}\big) \approx \frac{1}{\Delta z}\big(p_{1/2,1} - p_{1/2,0}\big) \approx \frac{1}{2\Delta z}(p_{0,1} + p_{1,1} - p_{0,0} - p_{1,0}), \tag{71b}$$

$$p_{1/2,1/2} := \frac{1}{2}(p_{0,1} + p_{1,0}), \tag{71c}$$

$$p_{0,1/2} := \frac{1}{2}(p_{0,0} + p_{0,1}). \tag{71d}$$

To handle the convolution term in (70), we define $\Delta t_0 := t^{1/2} - t^{-1/2}$, $p(t) := p(t, z_{1/2})$, $\mathring{c} := \mathring{c}\,(z_{1/2})$ and compute the integral

$$\begin{aligned}
\int_0^{t^{1/2}} \sum_{j=1}^{n+1} b_j e^{\alpha\mathring{c}\beta_j(t^{1/2}-t')} p(t')\,dt' &= \sum_{j=1}^{n+1} b_j \left(\int_0^{t^{1/2}} e^{\alpha\mathring{c}\beta_j(t^{1/2}-t')} p(t')\,dt' \right) \\
&= \sum_{j=1}^{n+1} b_j \left(\int_0^{t^{-1/2}} e^{\alpha\mathring{c}\beta_j(t^{1/2}-t')} p(t')\,dt' + \int_{t^{-1/2}}^{t^{1/2}} e^{\alpha\mathring{c}\beta_j(t^{1/2}-t')} p(t')\,dt' \right) \qquad (72) \\
&= \sum_{j=1}^{n+1} b_j \left(e^{\alpha\mathring{c}\beta_j \Delta t_0} \int_0^{t^{-1/2}} e^{\alpha\mathring{c}\beta_j(t^{-1/2}-t')} p(t')\,dt' + \int_0^{\Delta t_0} e^{\alpha\mathring{c}\beta_j(\Delta t_0-t')} p(t^{-1/2}+t')\,dt' \right).
\end{aligned}$$

If the grid is uniform in time, i.e., $\Delta t_{1/2} = \Delta t_0 =: \Delta t$, we can use the Simpson formula for the approximation of the second integral,

$$\begin{aligned}
&\int_0^{\Delta t} e^{\alpha\mathring{c}\beta_j(\Delta t-t')} p\big(t^{-1/2}+t'\big)\,dt' \\
&\quad \approx \frac{\Delta t}{6}\left(e^{\alpha\mathring{c}\beta_j \Delta t} p_{-1/2,1/2} + 4e^{\alpha\mathring{c}\beta_j \Delta t/2} p_{0,1/2} + p_{1/2,1/2}\right). \qquad (73)
\end{aligned}$$

In the case of a non-uniform grid with respect to time we apply a quadrature formula to the quadratic interpolation of $p_{-1/2,1/2}$, $p_{0,1/2}$, and $p_{1/2,1/2}$. From the calculations up to t^0 we already know an approximation of the first integral on the r.h.s. of (72),

$$A_j^{-1/2} \approx \int_0^{t^{-1/2}} e^{\alpha\mathring{c}\beta_j(t^{-1/2}-t')} p(t')\,dt'. \qquad (74)$$

Based on (72) we define the recurrence rule

$$\begin{aligned}
A_j^{1/2} &:= e^{\alpha\mathring{c}\beta_j \Delta t} A_j^{-1/2} + \frac{\Delta t}{6}\left(e^{\alpha\mathring{c}\beta_j \Delta t} p_{-1/2,1/2} + 4e^{\alpha\mathring{c}\beta_j \Delta t/2} p_{0,1/2} + p_{1/2,1/2}\right), \qquad (75) \\
A_j^{-1/2} &:= A_j^{1/2}.
\end{aligned}$$

Thus we get from (72)–(75)

$$\int_0^{t^{1/2}} \sum_{j=1}^{n+1} b_j e^{\alpha\mathring{c}\beta_j(t^{1/2}-t')} p(t',z)\,dt' \approx \sum_{j=1}^{n+1} b_j A_j^{1/2}. \qquad (76)$$

Note that the error in the approximation (76) occurs only because of (73); the recurrence rule (75) is stable due to nonpositive real parts of the coefficients β_j.

Combining (70), (71a)–(71d) and (76) we obtain

$$\begin{aligned}
p_{1,1} \approx \Bigg(&\frac{1}{2\Delta t}(p_{0,0}+p_{0,1}-p_{1,0}) + \frac{\mathring{c}}{2\Delta z}(p_{0,0}+p_{1,0}-p_{0,1}) \\
&- \frac{\mathring{c}}{2}\left(\alpha\vartheta + \frac{\alpha}{2}\right)(p_{0,1}+p_{1,0}) + \alpha^2\mathring{c}^2 \sum_{j=1}^{n+1} b_j A_j^{1/2} \Bigg) \Bigg/ \left(\frac{1}{2\Delta t} + \frac{\mathring{c}}{2\Delta z}\right). \qquad (77)
\end{aligned}$$

We see from (77) that the computational costs of defining the boundary value $p_{1,1}$ are proportional to the number of terms in the sum (69). An analysis of the examples from Fig. 4 and Table I in the next section shows that a highly accurate representation of the form

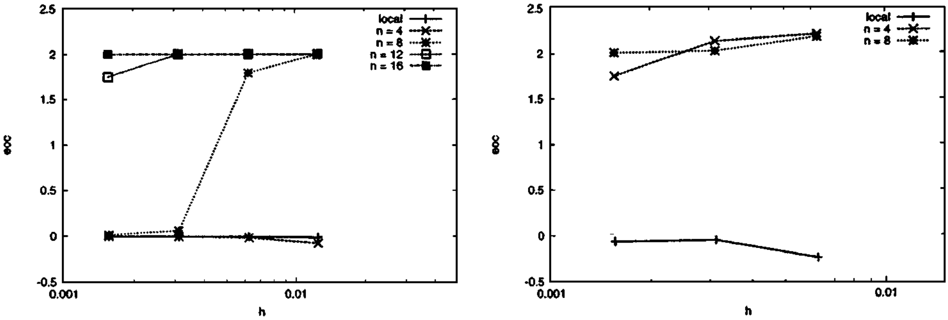

FIG. 4. Convergence rates for λ_1 at $t = 20$ (left) and λ_9 at $t = 100$ (right) with transparent boundary conditions on Γ_{bot} and Γ_{top}.

(69) can be achieved for comparably small values of n. (The approximation error in (69) is the second source of a residue in discretizing (39); this error is hidden in our analysis since we treated (70) instead of (39).) Note that estimates of the approximation (69) for the case of the wave equation with a constant speed of sound are contained in [3].

TABLE I
Errors and Convergence Rates

λ_1, $t = 20$: Transparent boundary conditions on Γ_{bot} and Γ_{top}

	Local		$n = 4$		$n = 8$		$n = 16$	
h	Error	eoc	Error	eoc	Error	eoc	Error	eoc
0.025000	0.171451		0.000346		0.000289		0.000289	
0.012500	0.172893	−0.01	0.000365	−0.08	0.000072	2.00	0.000072	2.00
0.006250	0.173592	−0.01	0.000369	−0.02	0.000021	1.79	0.000018	2.00
0.003125	0.174226	−0.01	0.000370	−0.00	0.000020	0.06	0.000005	2.00
0.001563	0.174542	−0.00	0.000370	−0.00	0.000020	0.02	0.000001	2.00

$n = 16$, $t = 100$: Transparent boundary conditions on Γ_{bot} and Γ_{top}

	λ_0		λ_1		λ_2		λ_3	
h	Error	eoc	Error	eoc	Error	eoc	Error	eoc
0.025000	0.000936		0.001475		0.003716		0.008199	
0.012500	0.000231	2.02	0.000357	2.05	0.000918	2.02	0.002013	2.03
0.006250	0.000061	1.91	0.000089	2.01	0.000230	2.00	0.000504	2.00
0.003125	0.000016	1.96	0.000023	1.97	0.000057	2.00	0.000127	1.99
0.001563	0.000004	1.95	0.000006	1.88	0.000014	2.00	0.000032	2.00

λ_9, $t = 100$: Transparent boundary conditions on Γ_{bot} and Γ_{top}

	Local		$n = 4$		$n = 8$		$n = 16$	
h	Error	eoc	Error	eoc	Error	eoc	Error	eoc
0.012500	0.056404		0.020772		0.020896		0.020896	
0.006250	0.066722	−0.24	0.004484	2.21	0.004604	2.18	0.004605	2.18
0.003125	0.068933	−0.05	0.001020	2.14	0.001130	2.03	0.001131	2.03
0.001563	0.071974	−0.06	0.000303	1.75	0.000280	2.01	0.000281	2.01

10. NUMERICAL TESTS

10.1. *Linear Problem for Single Fourier Harmonics*

For our first numerical tests we discretize (24) and compare the numerical solution obtained with our transparent boundary conditions (77) to a reference solution computed in a large domain for different values of λ. From (22) we have

$$q'(z) = -2\alpha q(z) = -2\alpha\vartheta\mathring{c}^{\,2}, \quad \left(\frac{q'}{q}\right)' \equiv 0. \tag{78}$$

Therefore (24) reads

$$\partial_{tt}^2\tilde{p}^\lambda - \mathring{c}^{\,2}\partial_{zz}^2\tilde{p}^\lambda - 2\alpha\vartheta\mathring{c}^{\,2}\partial_z\tilde{p}^\lambda + \lambda^2\mathring{c}^{\,2}\tilde{p}^\lambda = 0. \tag{79}$$

Using standard second order finite differences we get an explicit scheme for $\tilde{p}^\lambda$. We use the impulse

$$\tilde{p}^\lambda(0,z) = \tilde{p}_0^\lambda(z) := \begin{cases} e^{-\frac{4(z-5)^2}{1-(z-5)^2}} & (z \in [4,6]) \\ 0 & (z \in \mathbb{R}\backslash[4,6]) \end{cases} \tag{80}$$

and $\partial_t\tilde{p}^\lambda(0,\cdot) \equiv 0$ as initial conditions for our calculations. The parameters for the background solution are set to $a := 2.0$, $\alpha := 0.4$, and $\gamma := 5/3$. As a computational domain we use $\Omega_{comp} = [4,6]$. Thus the artificial boundaries Γ_{bot} and Γ_{top} are located at $z_b = 4$ and $z_t = 6$, respectively.

One of our main concerns is to perform stable and accurate long-time computations. However, the boundary condition on Γ_{bot} is a potential source of difficulty: According to the analysis in Section 8, the proposed transparent boundary condition (51) has no theoretical justification outside the initial time interval. From (57) we estimate $2t_b \approx 43$ as the critical simulation time. (Note that the modification introduced in Section 9.1 guarantees the stability of the approximation beyond this time.)

In the following we want to test the transparency of our boundary conditions numerically. We compare results computed in Ω_{comp} using our boundary conditions with a solution computed in the larger reference domain $[0, 10]$. The question remaining is which boundary conditions should be chosen for the reference domain. Using the equation for the characteristics (55), we can estimate that signals from Ω_{comp} reach the boundaries of the reference domain at $t \approx 17$. Therefore, up to the simulation time $t \approx 34$ no signal reflected at these boundaries influences the reference solution in Ω_{comp}. Thus the results shown in Figs. 5–7 are *independent* of the boundary conditions used for the reference domain. On the other hand, it is also evident from Section 8 that there is no reference domain large enough to rule out the possibility that reflected waves are generated which could influence the reference solution in Ω_{comp} for $t > 2t_b \approx 43$. In this case, we rely on a different test, which allows us to use our boundary conditions for the computation of the solutions in the reference domain. Indeed, transparency of a boundary condition means that the solution does not depend on the size of the domain. In the case of a numerical simulation this holds within an approximation error. If the difference between the solutions computed in Ω_{comp} and in the reference domain, using the same boundary conditions, converges to zero as $h \to 0$, we can conclude that these boundary conditions are in fact transparent.

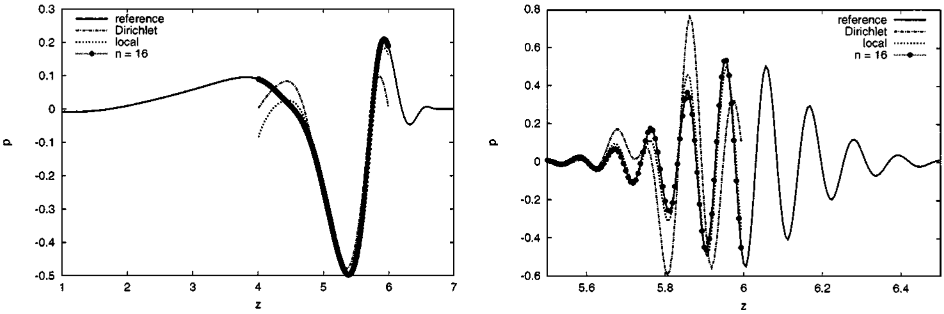

FIG. 5. Results for λ_1 at $t = 20$ (left) and λ_9 at $t = 35$ (right) with $h = 0.00625$ and different artificial boundary conditions; $\Omega_{comp} = [4, 6]$.

In the following we consider λ_1 and λ_9 as typical examples; the results for λ_0 are very similar to those for λ_1. We use the same grid spacing h for the calculations in Ω_{comp} and for the reference solutions. As a measure of error we use the maximal absolute value of the difference between these two solutions at the grid points in Ω_{comp} at a fixed time. The experimental order of convergence (eoc) is then computed as usual. The simulation times are chosen in such a way that noticeable disturbances pass through the boundaries of Ω_{comp} (see Fig. 5).

The results in Table I and Fig. 4 show that by choosing an appropriate value of n we achieve the expected second order accuracy with our boundary conditions. (n refers to the number of terms in the non-local convolution sum in (77); "local" means that this term is omitted, which leads to boundary conditions which are comparable to characteristic-based boundary conditions.) For λ_9 we obtain the optimal quadratic convergence (and constant errors on a fixed grid for increasing n) for $n = 8$. (If we think of reasonable grid sizes for two-dimensional simulations, even $n = 4$ suffices.) By contrast, we really "need" $n = 16$ in the case of λ_1. In the example considered this behavior is caused by varying influences from the bottom boundary: For λ_k with small index k (e.g., $k = 1$), the amplitudes of disturbances actually reaching Γ_{bot} are quite large, and therefore they strongly influence the overall errors; for larger indices k (e.g., $k = 9$) the disturbances at the bottom boundary are almost negligible. Moreover, Table I shows that the difference between the solutions in the computational and the reference domain is of the same order as the discretization error if we choose n compatible with the grid spacing h. Thus we conclude that our approximation yields transparent boundary conditions in the linear case even for long-time

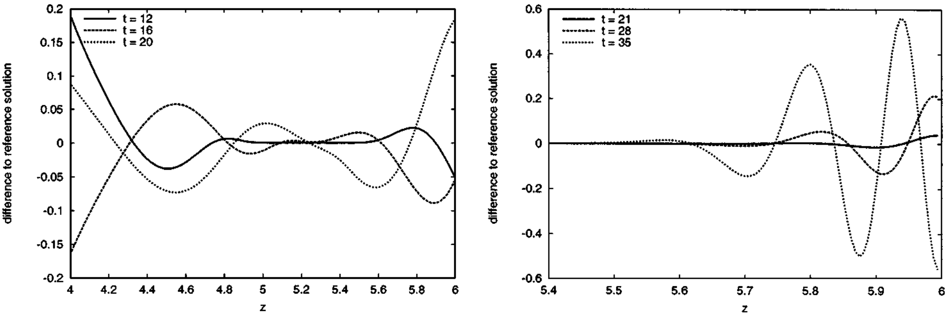

FIG. 6. Deviations from reference solution with Dirichlet conditions for λ_1 (left) and λ_9 (right) with $h = 0.00625$ in $\Omega_{comp} = [4, 6]$. For λ_9 we observe no activity for $z \in [4, 5.4]$.

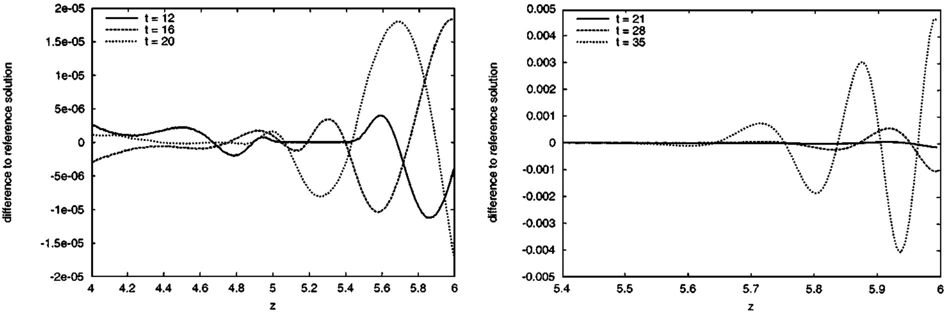

FIG. 7. Deviations from reference solution with transparent boundary conditions on Γ_{bot} and Γ_{top}: λ_1 for $n = 16$ (left) and λ_9 for $n = 8$ (right) with $h = 0.00625$ in $\Omega_{comp} = [4, 6]$. For λ_9 we observe no activity for $z \in [4, 5.4]$.

simulations. Note that the simulation breaks down if we do not use the modification discussed in Section 9.1.

In Fig. 5 we compare our results with those obtained using simple Dirichlet conditions (fixing the initial "zero disturbance" at the boundary). We see that the choice of appropriate boundary conditions is absolutely crucial for obtaining meaningful numerical solutions in the truncated domain. The evolution in time of the pointwise deviation from the reference solution is shown in Figs. 6 and 7: The errors in the solution with our transparent boundary conditions are smaller by several orders of magnitude than those obtained with Dirichlet conditions.

The tests presented show that the second order approximation of our boundary conditions, with a special treatment of the convolution kernels for the bottom boundary, works well for the linear wave problem (79) with an exponential speed of sound.

10.2. *One-Dimensional MHD Equations*

We now study how well our boundary conditions perform in calculations with the full nonlinear MHD equations. The transparent boundary conditions on Γ_{top} and Γ_{bot} are given by (41), (47)–(49) and (51), (59)–(61), respectively. First we examine the situation in one space dimension (assuming that the solution to (1a)–(3) does not depend on the space variable x). We discretize the MHD equations in Ω_{comp} by a first-order finite volume scheme, using the "simple Riemann solver" developed by Dai and Woodward [9] to calculate the fluxes. Due to the discretization errors in the finite volume scheme, our code was not capable of retaining the static background atmosphere. This caused severe problems in our calculations. Therefore we have added a simple fix to the finite volume algorithm, which enables our code to keep the background atmosphere exactly static. In one space dimension, the time evolution of the discrete solution now reads as follows:

$$\mathbf{U}_i^{n+1} := \mathbf{U}_i^n - \Delta t \mathbf{G}\big(\mathbf{U}_{i-1}^n, \mathbf{U}_i^n, \mathbf{U}_{i+1}^n\big) + \Delta t \mathbf{G}(\mathring{\mathbf{U}}_{i-1}, \mathring{\mathbf{U}}_i, \mathring{\mathbf{U}}_{i+1}). \tag{81}$$

$\mathbf{U}$ is the vector of conservative variables and $\mathring{\mathbf{U}}$ are the corresponding values of the background atmosphere; $\mathbf{G}$ describes the spatial discretization of (1a)–(1d) as in [11]. The additional term in (81) should be equal to zero since the background atmosphere is a static solution to (1a)–(3). Hence we have added a zero on the PDE level. Within the numerical scheme this term cancels out the errors induced by the averaging of the background atmosphere. The boundary conditions (41), (47)–(49), (12a), and (12b) for Γ_{top} and (51), (59)–(61), (12a), and (12b) for Γ_{bot} are discretized by a second order finite difference scheme similar to the one described in Section 9.2. The values obtained are used as ghost cell values in the finite volume scheme.

As already noted, the background atmosphere is uniquely defined by the values of $\gamma > 1, \alpha > 0, a > 0$ (see Section 6). For the results shown in this section we choose $\gamma := \sqrt{3}, \alpha := 0.1, a := 4.2$. This results in a slower decay of the density compared to the atmosphere used in the preceding section. In our applications we study magnetic flux tubes. These are strong local magnetic field concentrations normal to the computational (x, z)-plane, with an additional magnetic field tangential to the tube boundary (see Section 1 and [27]). Characteristic properties of this setting are a lower density and a lower gas pressure within the flux tube. The gas pressure is chosen in such a way that the total pressure (gas pressure plus magnetic pressure) in the flux tube is balanced with the total pressure of the surrounding atmosphere. With these initial conditions in mind, we test our transparent boundary conditions for the setting

$$\rho\,(0, z) := \begin{cases} \mathring{\rho}(z + 1.5) & (z \in [0.2, 0.4]), \\ \mathring{\rho}(z) & (\text{otherwise}), \end{cases} \tag{82a}$$

$$u_z(0, z) := 0.025\,\mathring{c}\,(0.3)e^{-100(z-0.3)^2}, \tag{82b}$$

$$B_x(0, z) := \begin{cases} 0.005\frac{z-0.3}{0.1} & (z \in [0.2, 0.4]), \\ 0 & (\text{otherwise}), \end{cases} \tag{82c}$$

$$p(0, z) := \mathring{p}\,(z) - \frac{B_x(0, z)^2}{8\pi}, \tag{82d}$$

and homogeneous initial conditions for all other quantities. These initial conditions lead to a rise of the “flux tube” located at [0.2, 0.4]. Waves of small amplitude are generated which move at a far higher speed than this density “perturbation” (see Fig. 8).

As in the preceding section we compare results computed in a small domain using artificial boundaries with a reference solution obtained in a much larger domain (using the

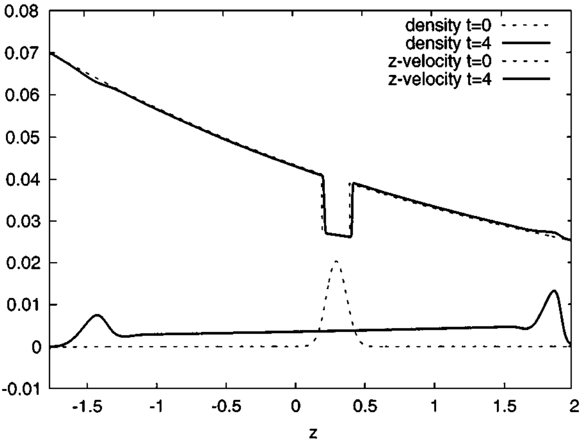

FIG. 8. Reference solution: Density (top) and velocity (bottom) at time $t = 0$ and $t = 4$ calculated with $h = 0.001$ in the domain $[-5, 6]$. Only that part of the reference domain is shown which has been influenced by the initial perturbations in $\Omega_{comp} = [0, 1]$. At time $t = 4$ two waves here moved through the boundaries of Ω_{comp}, whereas the “flux tube” has moved only slightly upward.

same grid spacing h). We choose $\Omega_{comp} = [0, 1]$ and $[-9, 11]$ as reference domain and compare the performance of different artificial boundary conditons for the calculations in Ω_{comp}:

Dirichlet boundary conditions:

$$\partial_t(\rho, \mathbf{u}, \mathbf{B}, p)|_{\Gamma_{bot} \cup \Gamma_{top}} = 0. \tag{dbc}$$

Neumann boundary conditions:

$$\partial_t \partial_z(\rho, \mathbf{u}, \mathbf{B}, p)|_{\Gamma_{bot} \cup \Gamma_{top}} = 0. \tag{nbc}$$

local transparent boundary conditions:

$$\begin{aligned} &\text{(41) and (51) without the convolution term;} \\ &\text{(47)–(49) and (59)–(61).} \end{aligned} \tag{tbc–loc}$$

transparent boundary conditions:

$$\text{(41), (47)–(49), (51), (59)–(61).} \tag{tbc}$$

All four conditions are exact as long as no perturbations have reached the boundaries. We always use identical boundary conditions on Γ_{bot} and Γ_{top}.

In Fig. 9 we compare solutions computed in Ω_{comp} with solutions obtained in larger domains using (tbc) and (dbc). We have refrained from including the (nbc) results since they were much worse. The results with (tbc–loc) are close to the solutions computed with (dbc) (also see Fig. 10). For our application, the position and shape of the “flux tube” is crucial. Only our transparent boundary conditons (tbc) are capable of reproducing this part of the solution with a high degree of accuracy (cf. Fig. 9 (left)).

In Fig. 10 we compare the solutions in Ω_{comp} at fixed times t with the reference solutions using the sum of the L^1-distances in the variables $\rho(t, \cdot)$, $\mathbf{u}(t, \cdot)$, $\mathbf{B}(t, \cdot)$, and $p(t, \cdot)$. For the

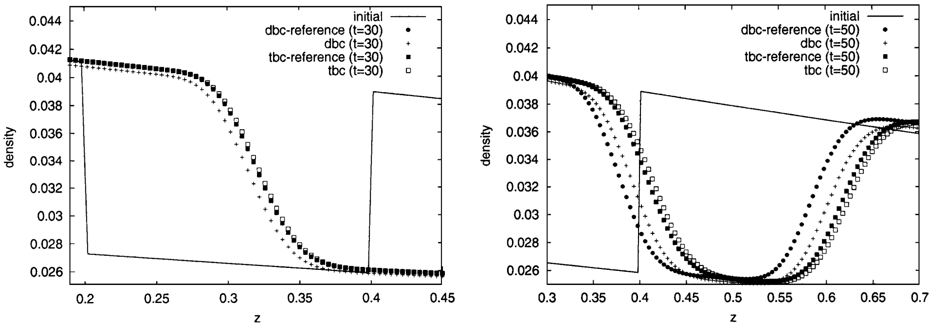

FIG. 9. Comparison of the solutions in Ω_{comp} with two reference solutions computed with (dbc) and with (tbc) using $h = 0.004$. Left ($t = 30$): The reference solutions are indistiguishable and the solution in Ω_{comp} with (tbc) is very close to the reference solutions. Right ($t = 50$): The solution with (tbc) in Ω_{comp} is still close to the reference solution with (tbc). This demonstrates that our conditions are transparent even in the nonlinear case. Both solutions with (dbc) differ significantly from the (tbc) solutions and even from each other.

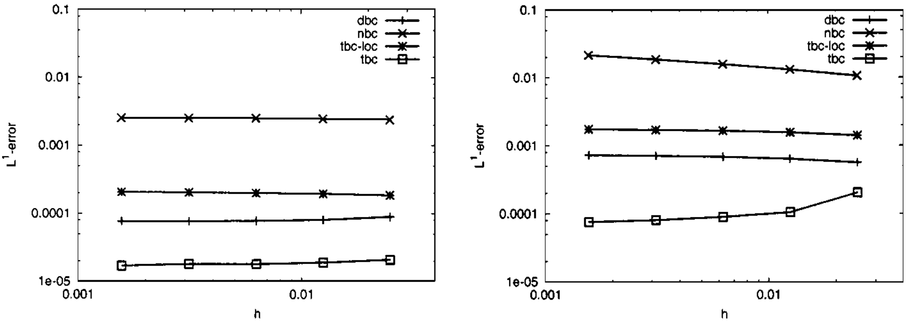

FIG. 10. The L^1-norm of the difference between the reference solution and the solutions in Ω_{comp} is shown for different values of the grid spacing h. The reference solution and the solutions in Ω_{comp} are calculated using identical grid spacing. In the left figure the comparison is made at time $t = 25$, in the right figure at time $t = 75$.

computation of the reference solution we use our boundary conditions, although one cannot assume that they are genuinely transparent in the nonlinear case. The linearization process results in an unavoidable error. Thus we cannot expect the solution obtained in Ω_{comp} to converge to the reference solution. The boundary conditions for the reference domain can influence the reference solution in Ω_{comp} for $t > 28$. Therefore, the results in Fig. 10 (left) are independent of the conditions imposed on the boundaries of the reference domain. For this setting of the atmosphere we compute $2t_b \approx 48$. Hence for $t > 48$ the values in Ω_{comp} of *any* reference solution may depend on the boundary conditions. In order to check whether the results in Fig. 10 (right) *actually* depend on these conditions, we have compared them with the corresponding results for the reference domain $[-15, 15]$ with both (tbc) and (dbc). It is worth noting that we have found no differences in these cases, which does not hold if we use (dbc) instead of (tbc) for the original reference domain $[-9, 11]$ (see also Fig. 9 (right)).

We observe that the error induced by (tbc) is up to one order of magnitude smaller than for any of the other approaches. Moreover, using (tbc) the error is decreased slightly by grid refinement, whereas it grows for the other boundary conditions. Thus we can conclude that even in the nonlinear case our boundary conditions lead to a stable and accurate approximation of the solution in Ω_{comp}.

10.3. *Two-Dimensional MHD Equations*

For our two-dimensional test calculations we use the same setting as for the one-dimensional calculations; the only modification of (82a)–(82d) is a sinusoidal x-dependency in the initial values for u_z:

$$u_z(0, x, z) := (\cos(2\pi(x - 0.5)) + 1)0.025\,\mathring{c}(0.3)e^{-100(z-0.3)^2}. \tag{83}$$

For the computational domain we choose the unit square $\Omega_{comp} := [0, 1] \times [0, 1]$. The initial disturbance in the vertical velocity u_z causes the “flux tube” to rise faster in the middle of the domain. This leads to the development of a “mushroom” shape similar to a classical Rayleigh–Taylor instability (see Fig. 12). As in the 1D simulations two high speed waves move upward and downward through the atmosphere; cf. Figs. 8 and 11.

We again compare the results in Ω_{comp} using the four boundary conditions described in the preceding section on Γ_{bot} and Γ_{top} with a reference solution. As reference domain we

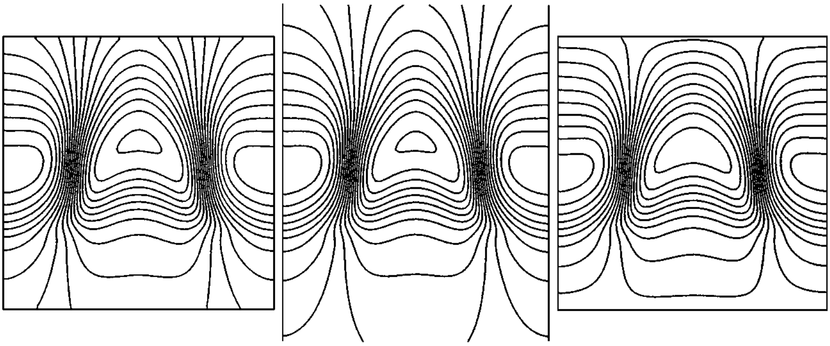

FIG. 11. Isolines of the vertical velocity for the 2-D problem in Ω_{comp} with transparent boundary conditions (left) and Dirichlet boundary conditions (right). The middle picture shows the reference solution in Ω_{comp}. All solutions are computed with $h = 0.025$. At the displayed time $t = 25$ the "flux tube" has not yet reached Γ_{top} . Note that small perturbations have already reached the top and bottom boundaries via acoustic waves.

take $[0, 1] \times [9, 11]$, which is 20 times larger than Ω_{comp}. We use a finite volume scheme on a Cartesian grid analogous to the one described in the preceding section. The mesh is 80×80 for Ω_{comp} and 80×1600 for the reference domain. Thus both grids match each other in Ω_{comp}. Based on our experience described in Section 10.1, we use approximations of the convolution kernels—see (77)—with $n = 14$ for Γ_{bot} and $n = 8$ for Γ_{top}; we take the non-local term only for the first 20 Fourier harmonics (see discussion at the beginning of Section 9). For λ_0 we use $M = 18$, whereas $M = 14$ is sufficient for the remaining Fourier modes. Since the background atmosphere is the same as in the previous example, we again find $2t_b \approx 48$. As before, at $t \approx 28$ waves reflected at the boundaries of the reference domain may have reached Ω_{comp}.

Figure 11 shows an isoline representation of the vertical velocity at $t = 25$. On the left and on the right we see the solutions computed in Ω_{comp} with (tbc) and (dbc), respectively. The middle picture is the reference solution. At this moment, disturbances have moved through the top and the bottom boundary. Note that the (tbc) result can hardly be

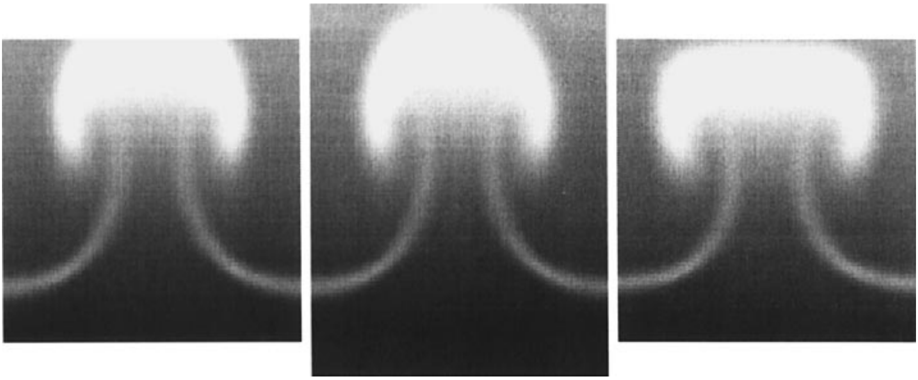

FIG. 12. Density plot of the solution to the 2-D problem in Ω_{comp} with transparent boundary conditions (left) and Dirichlet boundary conditions (right). The middle picture shows the reference solution in Ω_{comp}. All solutions are shown at $t = 35$ with $h = 0.025$.

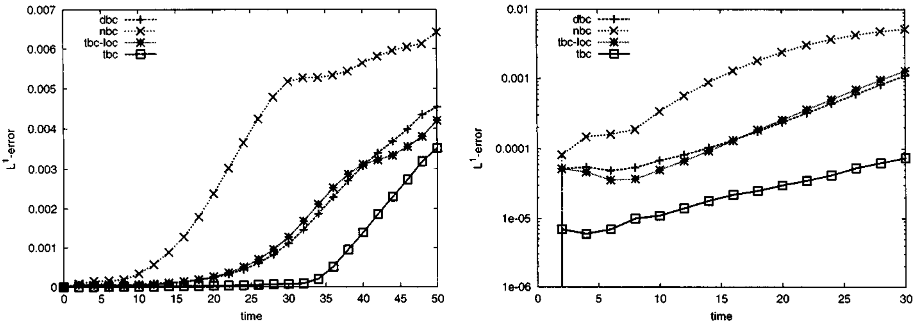

FIG. 13. L^1-norm of the difference between the reference solution and the solutions in Ω_{comp} versus time for a 2-D calculation with $h = 0.025$. On the left the development of errors is shown for the whole time simulated; on the right only for the first part of the calculation using a logarithmic error axis. Note that the "flux tube" reaches Γ_{top} at $t \approx 30$ (see Fig. 12).

distinguished from the reference solution. On the other hand, the (dbc) solution is noticeably different.

In Fig. 12 (middle) the density of the reference solution is shown together with the solutions in Ω_{comp} with transparent boundary conditions (left) and Dirichlet boundary conditions (right). At this time, the "mushroom-shaped" region with lower density has reached Γ_{top} and begins to move through the boundary. The solution obtained in Ω_{comp} with (tbc) still accurately reproducing the shape and position of the "mushroom," whereas the Dirichlet conditions lead to the wrong shape. Of the three boundary conditions (dbc, nbc, tbc–loc) we use to verify the quality of our transparent ones, the Neumann boundary conditions (nbc) yield by far the worst results, while the results using the other two techniques are approximately the same. This can be seen in Fig. 13. As in our 1-D calculations, the errors for (tbc)—up to the point where the low density region reaches $\Gamma_{top}(t \approx 30)$—are one order of magnitude smaller than the errors produced by the other boundary conditions. Beyond that time we still get the best solution with (tbc).

11. CONCLUSIONS

We have proposed transparent boundary conditions for problems governed by the MHD equations with an exponential equilibrium atmosphere as background solution in the far field. These conditions are obtained by linearizing the MHD system about the background atmosphere. They permit the use of a truncated computational domain with artificial horizontal boundaries. We have proven that these boundary conditions are exact for the linear system of perturbations. In numerical tests for the pressure perturbation we have obtained the expected quadratic convergence. The results for the full nonlinear MHD system in 1D and 2D are still good: the deviations from the reference solution are up to one order of magnitude smaller than those obtained with Dirichlet, Neumann, or characteristic-based boundary conditions.

Although our transparent boundary conditions involve a nonlocal convolution term with respect to time, we are able to obtain a numerical algorithm which is *local* with respect to time. Therefore, the costs for the numerical evaluation of the boundary conditions are almost negligible: in our 2-D example it took less than 1% of the overall CPU time (see Fig. 14).

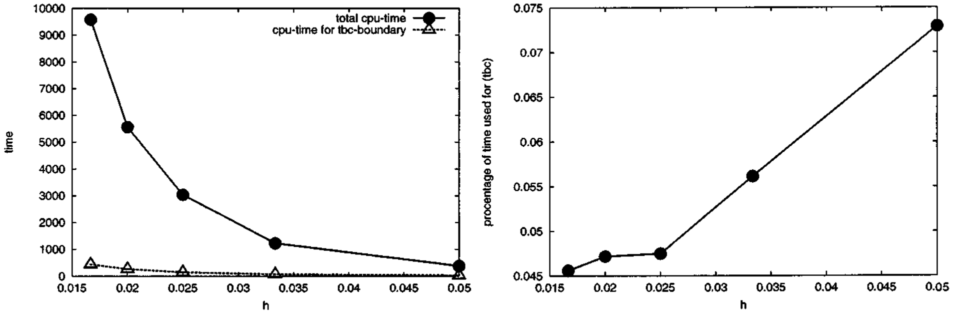

FIG. 14. Time used for the whole 2-D calculation in Ω_{comp} for different grid sizes in comparison to the time required for the calculation of the boundary values with (tbc).

The extensive tests presented show that the proposed conditions are very effective and efficient. In a forthcoming paper we will focus on the advantage these conditions offer for multi-dimensional applications in solar physics.

APPENDIX: EXAMPLE OF MAPLE PROGRAM

```
Digits    :=100;  degp      :=16;
koef_a    :=2;    koef_alpha:=0.4;
koef_gamma:=5/3;  koef_theta:=1/(koef_gamma-1);
n:=1; p_lambda:=evalf(2*Pi*n);
nu:=evalf(sqrt((p_lambda/koef_alpha)^2+koef_theta^2));
an:=10^degp;
ak:= proc(s)
  an*(-s*BesselK(nu+1,s)/BesselK(nu,s) + nu + s + 1/2)
end;
smax:=4*nu; infolevel[chebyshev]:=3;
c2:=chebyshev(ak,s=10^(-10)..smax, 10^(-2*degp-1));
readlib(unassign): unassign(T);
c3:=convert(c2,ratpoly,degp,degp+1);
with(numapprox):with(orthopoly):
fa:=confracform(subs(T=orthopoly[T],c3));
nfa:=normal(fa/an);
Digits:=15;
# plot(10^(12)*evalf((ak(s))/an-nfa(s)),s=0..200);
readlib(laplace): unassign('t');
k16:=invlaplace(nfa,s,t);
plot(k16(t),t=0..2);
```

ACKNOWLEDGMENTS

We thank the referees for their valuable comments, which helped us improve this paper.

REFERENCES

1. S. Abarbanel and D. Gottlieb, On the construction and analysis of absorbing layers in CEM, *Appl. Numer. Math.* **27**(4), 331 (1998).

2. M. Abramowitz and I. A. Stegun (Eds.), *Handbook of Mathematical Functions with Formulas, Graphs, and Mathematical Tables.* 10th printing, with Corr. (Wiley, New York, 1972, National Bureau of Standards. A Wiley-Interscience Publication).
3. B. Alpert, L. Greengard, and T. Hagstrom, Rapid evaluation of nonreflecting boundary kernels for time-domain wave propagation, *SIAM J. Numer. Anal.* **37**, 1138 (2000).
4. A. Bayliss and E. Turkel, Far field boundary conditions for compressible flows, *J. Comput. Phys.* **48**, 182 (1982).
5. J.-P. Berenger, A perfectly matched layer for the absorption of electromagnetic waves, *J. Comput. Phys.* **114**(2), 185 (1994).
6. P. Caligari, F. Moreno-Insertis, and M. Schüssler, Emerging flux tubes in the solar convection zone. I: Asymmetry, tilt, and emergence latitude, *Astrophys. J.* **441**(2), 886 (1995).
7. P. Caligari, M. Schüssler, and F. Moreno-Insertis, Emerging flux tubes in the solar convection zone. II: The influence of initial conditions, *Astrophys. J.* **502**, 481 (1998).
8. R. A. Chevalier, The stability of an accelerating shock wave in an exponential atmosphere, *Astrophys. J.* **359**, 463 (1990).
9. W. Dai and P. R. Woodward, A simple Riemann solver and high-order Godunov schemes for hyperbolic systems of conservation laws, *J. Comput. Phys.* **121**, 51 (1995).
10. A. Dedner, D. Kröner, I. L. Sofronov, and M. Wesenberg, Absorbing boundary conditions for astrophysical MHD simulations, in *Godunov Methods: Theory and Applications Edited Review*, edited by E. F. Toro (Kluwer Academic/Plenum, 2001).
11. A. Dedner, C. Rohde, and M. Wesenberg, *A MHD*-simulation in solar physics, in *Finite Volumes for Complex Applications II: Problems and Perspectives* edited by R. Vilsmeier, F. Benkhaldoun, and D. Hänel (Hermès Science Publications, Paris, 1999), pp. 491–498.
12. G. Doetsch, *Guide to the Applications of the Laplace and Z-Transforms*, 2nd ed. (Van Nostrand Reinhold, London, 1971).
13. T. Emonet and F. Moreno-Insertis, The physics of twisted magnetic tubes rising in a stratified medium: Two-dimensional results, *Astrophys. J.* **492**, 804 (1998).
14. B. Engquist and A. Majda, Numerical radiation boundary conditions for unsteady transonic flow, *J. Comput. Phys.* **40**, 91 (1981).
15. Y. Fan, E. G. Zweibel, and S. R. Lantz, Two-dimensional simulations of buoyantly rising, interacting magnetic flux tubes, *Astrophys. J.* **493**, 480, (1998).
16. D. Givoli, Non-reflecting boundary conditions, *J. Comput. Phys.* **94**(1), 1 (1991).
17. M. J. Grote and J. B. Keller, Nonreflecting boundary conditions for time-dependent scattering, *J. Comput. Phys.* **127**(1), 52 (1996).
18. M. J. Grote and J. B. Keller, Nonreflecting boundary conditions for Maxwell's equations, *J. Comput. Phys.* **139**(2), 327 (1998).
19. M. J. Grote and J. B. Keller, Exact nonreflecting boundary condition for elastic waves, SIAM *J. Appl. Math.* **60**, 803 (2000).
20. R. Grover and J. W. Hardy, The propagation of shocks in exponentially decreasing atmospheres, *Astrophys. J.* **143**, 48 (1966).
21. T. Hagstrom, Radiation boundary conditions for the numerical simulation of waves, in *Acta Numerica*, edited by A. Iserles (Cambridge Univ. Press, Cambridge, 1999), Vol. 8, pp. 47–106.
22. G. A. Korn and T. M. Korn, *Mathematical Handbook for Scientists and Engineers: Definitions, Theorems, and Formulas for Reference and Review*, McGraw–Hill Handbook, (McGraw–Hill, New York, 1961).
23. D. Kröner, Absorbing boundary conditions for the linearized Euler equations in 2-D, *Math. Comput.* **57**(195), 153 (1991).
24. A. Nordlund and R. F. Stein, 3-D simulations of solar and stellar convection and magnetoconvection, *Comput. Phys. Commun.* **59**(1), 119 (1990).
25. P. G. Petropoulos, Reflectionless sponge layers as absorbing boundary conditions for the numerical solution of Maxwell equations in rectangular, cylindrical, and spherical coordinates, *SIAM J. Appl. Math.* **60**(3), 1037 (2000).

26. V. S. Ryaben'kij and S. V. Tsynkov, Artificial boundary conditions for the numerical solution of external viscous flow problems, *SIAM J. Numer. Anal.* **32**(5), 1355 (1995).
27. M. Schüssler, Magnetic buoyancy revisited—Analytical and numerical results for rising flux tubes, *Astronom. Astrophy.* **71**(1/2), 79 (1979).
28. I. L. Sofronov, Conditions for complete transparency on the sphere for the three-dimensional wave equation, *Russ. Acad. Sci. Dokl. Math.* **46**(2), 397 (1992). English. Russian original; translation from *Dokl. Akad. Nauk, Ross. Akad. Nauk* **326**(6), 953 (1992).
29. I. L. Sofronov, Artificial boundary conditions of absolute transparency for two- and threedimensional external time-dependent scattering problems, *Eur. J. Appl. Math.* **9**(6), 561 (1998).
30. I. L. Sofronov, Non-reflecting inflow and outflow in a wind tunnel for transonic time-accurate simulation, *J. Math. Anal. Appl.* **221**(1), 92 (1998).
31. S. V. Tsynkov, Numerical solution of problems on unbounded domains. A review, *Appl. Numer. Math.* **27**(4), 465 (1998).
32. E. Turkel and A. Yefet, Absorbing PML boundary layers for wave-like equations, *Appl. Numer. Math.* **27**(4), 533 (1998).